附件一

計畫總主持人／共同主持人之研究成果

1.近五年內最具代表性之著作、專利或技術報告抽印本或影印本一至五件。

Journal of The Electrochemical Society, **150** (5) C320-C324 (2003)
0013-4651/2003/150(5)/C320/5/$7.00 © The Electrochemical Society, Inc.

Characterization and Formation Mechanism of Macroparticles in Arc Ion-Plated CrN Thin Films

M. H. Shiao, Z. C. Chang, and F. S. Shieu[*,z]

Department of Materials Engineering, National Chung Hsing University, Taichung 402, Taiwan

The microstructure and chemistry of macroparticles in CrN films prepared by an arc ion-plating method on AISI 304 stainless steel was characterized by an energy filtering transmission electron microscope (TEM) equipped with an electron energy loss spectroscopy (EELS) detector. The surface morphology of the CrN coatings with macroparticles was examined by a high-resolution field emission scanning electron microscope (SEM). SEM observation shows that the macroparticles lie on craters and protrude out of the coating surface. Cross-sectional and plan-view TEM results reveal that the macroparticles are bud shape, which has the Cr metal located at the bottom center and surrounded by a chromium nitride layer. Quantitative EELS analysis of a macroparticle from the core region to the outer shell shows that the nitrogen and oxygen concentrations in the macroparticle increase from 17.7 to 38 atom % and 7.7 to 9.5 atom %, respectively. On the basis of the analysis, a model describing the formation of macroparticles in the arc ion-plated CrN coatings is proposed.
 [DOI: 10.1149/1.1564107]

Manuscript submitted July 16, 2002; revised manuscript received November 8, 2002. Available electronically March 20, 2003.

The arc ion-plating technique with features of high ionization ratio and ion kinetic energy, produces hard coatings of high packing density and good adhesion. The higher deposition rate of arc ion plating than other physical vapor deposition (PVD) methods such as ion beam sputtering makes it attractive for cutting tool, semiconductor, and decorative industries. However, the presence of macroparticles in the coatings lowers erosion and corrosion resistances, and reduces the luster of the coatings. A very good review of the growth defect formation in cathodic arc evaporated coatings was given by Aharonov *et al.*,[1] who first carried out a systematic study of the effect of bias voltage characteristics, such as the amplitude, frequency, and duty cycle, on the evolution of defects in TiN coatings.

Many studies of arc ion-plating technology in recent years have dealt with the reduction of macroparticles by manipulating the deposition parameters such as arc current and partial pressure of the reactive gases,[2,3] or by adding a cylindrical filter to the deposition systems.[4–6] Generally, the macroparticles are composed only of the metal phase.[7,8] This model can account partly for the poor coating properties and performance that the arc ion-plated nitrides have exhibited. However, the model cannot explain why there is no contrast between the macroparticles and the matrix of the nitride coating, of which the average atomic number is different, when examined by X-ray mapping and backscattered electron image (BEI) in a scanning electron microscope (SEM).

In contrast to the coating properties and processing manipulation, relatively few reports have focused on the microstructure and chemistry of macroparticles in an arc ion-plated nitride coating. In our previous study[9,10] of the macroparticles in TiN and TiAlN coatings by cross-sectional transmission electron microscopy (TEM), a formation mechanism of the macroparticles in arc ion-plated nitride coatings was proposed. In this paper, characterization of the macroparticles in arc ion-plated CrN coatings was carried out by cross-sectional and plan-view TEM along with electron energy loss spectroscopy (EELS). Surface morphology and composition of the CrN coatings with macroparticles were examined by SEM in the secondary electron image (SEI) and BEI modes. On the basis of SEM and TEM analyses, an answer to the above-mentioned analytical question is provided and the formation mechanism of macroparticles in the arc ion-plated CrN coatings is discussed.

Experimental

AISI 304 stainless steel specimens whose surface had an average roughness of $R_a = 0.18$ μm, were used as substrates for CrN coatings. After a protective plastic cover was removed from the specimens, the steel substrates were cleaned thoroughly in an ultrasonic bath cleaner with acetone. A schematic diagram of the arc ion-plating system is shown in Fig. 1. The distance of the substrates from the Cr cathode, which was placed on the upper section of the vacuum chamber, was about 150 mm. The purity of the Ar and N_2 gases used was 99.9% and that of the Cr target was 99.99%. The base pressure of the vacuum chamber before operation of the system was about 7×10^{-3} Pa.

Prior to deposition, the surface of the substrates was further cleaned by Ar ion bombardment with an energy of 800 eV for 30 min and the temperature of the steel substrates was gradually raised to 350°C. The pressure of the Ar gas during ion bombardment was about 1.33 Pa. Subsequently, deposition of Cr began at a substrate bias of 400 V with an arc current of 70 A for 1 min. Deposition of CrN was initiated by introducing N_2 gas at a pressure of 2.66 Pa into the vacuum chamber, and the substrate bias was reduced to 150 V. The deposition time of the CrN coatings was 60 min, and the arc current was controlled at 70 A. Under this condition, the deposition rate was estimated to be about 50 nm/min, which gave a film thickness of about 3 μm after 60 min deposition.

The surface morphology of the CrN coatings with macroparticles was examined by a Hitachi S4100 high-resolution field emission scanning electron microscope. In addition to the SEI, the BEI was also used to investigate the image contrast between macroparticles and the matrix of the nitride coatings.

Two types of thin specimens, *i.e.*, plan-view and cross-sectional, were made for TEM investigation. The plan-view specimen was prepared first by sectioning the CrN-coated steel sheet into a 4×4 mm square, and then grinding and polishing from the steel side down to about 30 μm thick, and then cut into a 3 mm disk from the square for subsequent ion milling. The cross-sectional specimen was prepared by gluing two 5 × 5 mm square specimens face-to-face, and then cutting perpendicular to the coating/substrate interface into slices about 1 mm thick. After grinding and polishing down to about 30 μm thick, the thin specimen was attached to a Cu grid for ion milling.

Ion milling was carried out using a BAL-TEC RES 010 ion mill, operated at 5 kV, using a single-side sample holder at a milling angle of 15 and 7° for the plan-view and cross-sectional specimens, respectively. For the plan-view specimen, the milling process was initiated from the metal side until perforation. To examine the inner part of the macroparticles, the specimen was further ion milled from the coating side to reveal the subsurface microstructure. For the cross-sectional specimen, special care was taken to reduce the preferential etching due to different sputtering rates of the coating and the steel by using an oscillating system, by which the ion beam was directed mainly perpendicular to the interface.

* Electrochemical Society Active Member.
[z] E-mail: fsshieu@dragon.nchu.edu.tw

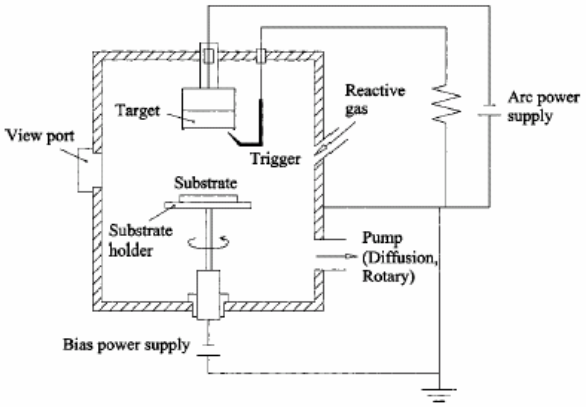

Figure 1. A schematic diagram of the arc ion plating system.

Characterization of the nitride coatings was carried out by an energy-filtering TEM, Zeiss EM 902 A, operated at 80 kV. With the in-column magnetic prism (energy filter of the prism/mirror/prism-type according to Castaing/Henry/Ottensmeyer) engaged, the contrast and resolution of the image and diffraction pattern can be improved greatly by choosing only the elastically scattered electrons for observation with the energy selecting slit below the spectrometer. The energy resolution in the electron spectroscopic imaging was better than 25 eV. The electron detector for EELS was a photomultiplier tube (PMT) with an energy resolution of 1.5 eV mounted below the final fluorescent imaging screen. The microscope was operated in the spectrum mode for the EELS recording.

Results

A typical SEM micrograph showing CrN macroparticles is displayed in Fig. 2, in which the specimen was tilted 40° to give a three-dimentional perspective. The apparent size of the macroparticle is about 3 μm. The macroparticle laid in a crater, had a conical shape and protruded out of the CrN coating surface. Top-view SEM of the macroparticles in SEI and BEI modes are shown in Fig. 3. It is readily seen that the contrast between the macroparticles and the CrN coating is relatively weak in the BEI mode. This contradicts the assumption that the macroparticles are composed only of the Cr metal phase; metallic Cr macroparticles should be much brighter, due to a higher backscatter coefficient, than the CrN matrix in the BEI.

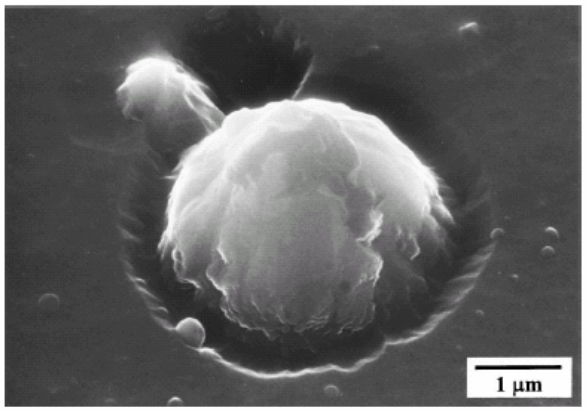

Figure 2. SEM micrograph of a macroparticle in the CrN coating.

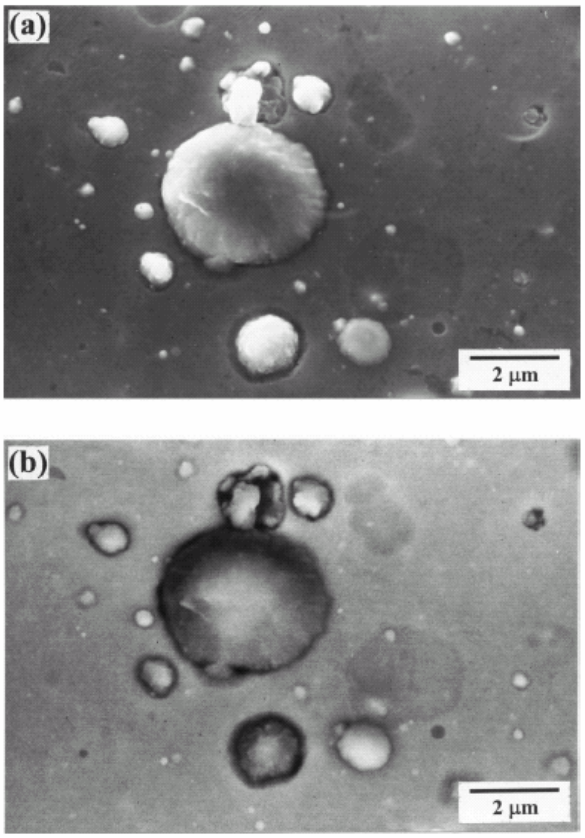

Figure 3. Top-view SEM micrographs of macroparticles in a CrN coating using (a) SEI and (b) BEI imaging mode.

A cross-sectional TEM micrograph of a CrN macroparticle protruding out of the CrN coating surface is shown in Fig. 4. The apparent size of the macroparticle is about 0.85 μm. The macroparticle is bud shaped. A Cr droplet is located at the bottom center surrounded by a nonuniform layer with a columnar structure radiating from the center. A flattened torus void is present beneath the macroparticle. An enlargement of the lower-left corner of the macroparticle is shown in Fig. 4b, in which, by close examination, a thin layer with microstructure different from the central droplet can be identified.

To reveal the inner microstructure of the macroparticle by plan-view TEM, the thin specimen was further ion-milled from the coating side after perforation, as described previously in the experimental procedure. Figure 5 shows the plan-view bright-field image and selected area diffraction (SAD) patterns of a macroparticle. The chromium nitride surrounding the central droplet exhibits a columnar structure and radiates out of the droplet. The very high contrast of the core structure in Fig. 5a is caused by very strong electron scattering of Cr in the [011] zone axis, as indicated in Fig. 5b. When the selected area aperture was located at the rim of the CrN macroparticle, which covers the nitride coating and part of the Cr droplet, the SAD pattern was obtained as shown in Fig. 5c. CrN reflections were identified in addition to the Cr metal phase.

The EELS spectra of the center Cr grain and the surrounding CrN layer of the macroparticle are shown in Fig. 6. For the Cr grain shown in Fig. 6a, the $L_{2,3}$ edges of Cr located at 575 eV are readily seen, but the K edge of O located at 532 is barely observed. Near the inner region of the CrN layer, the K edge of N located at 401 eV was detected in addition to the Cr and O peaks, as shown in Fig. 6b. The

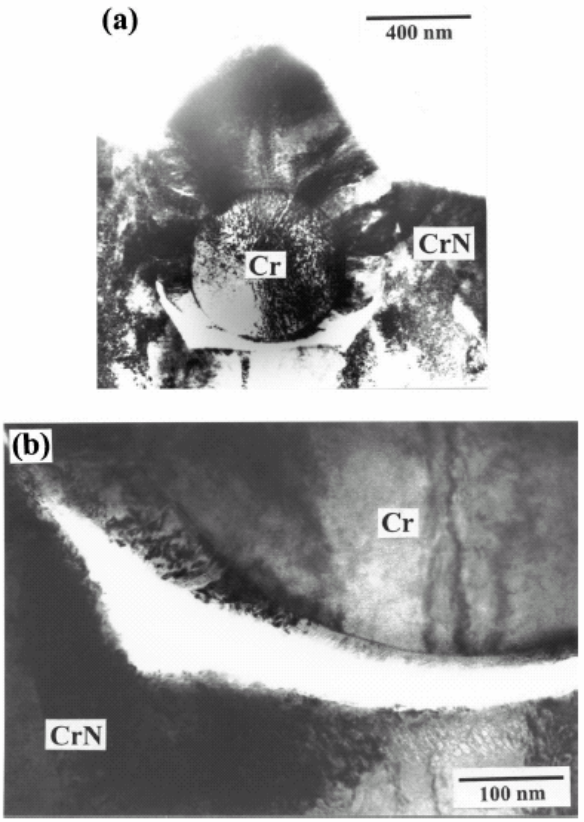

Figure 4. (a) Cross-sectional TEM micrograph of a macroparticle inlaid in an arc ion-plated CrN coating. (b) Enlargement of the lower-left corner of the macroparticle.

EELS spectrum of the outer shell CrN is shown in Fig. 6c. The intensities of O and N increase as the probed areas approach from the inner to the outer shell of the macroparticle.

Small Cr droplets tend to have a spherical shape, as shown in Fig. 4 and 5, in which the radii of the central Cr droplets are 0.29 and 0.43 μm, respectively. For larger droplets, *e.g.*, the metal droplet in the center of Fig. 7, they have a flat-bottomed or semielliptical shape. In addition, when the macroparticles spalled off the coating surface due to mechanical impacts or thermal treatments, pinholes were observed in the coating as shown in Fig. 8.

Discussion

Formation of macroparticles in the CrN coatings.—Generation of ions, electrons, neutrals, and droplets on the cathode surface in an arc evaporation system has been discussed extensively, *e.g.*, see Ref. 1,2,11-14. During deposition various radii of droplets, from submicrometers to tens of micrometers, are emitted at various angles from the Cr cathode surface and the local temperature on the cathode surface may be higher than the melting point of the Cr cathode (1863°C).[15] The emission angle of the Cr droplets from the cathode surface tends to decrease with increasing droplet size.[2,12,16]

Before a Cr droplet is emitted from the cathode surface, the steel substrate may have been deposited with CrN for a period of time, as depicted in Fig. 9a and b. Cheng *et al.*[8] used a thermal analysis method to analyze the temperature of Ti droplets with different sizes vs. the distance to the cathode. Their results showed that the temperature of the Ti droplets with a radius smaller than 2 μm, decreased considerably, down to less than the melting point of Ti

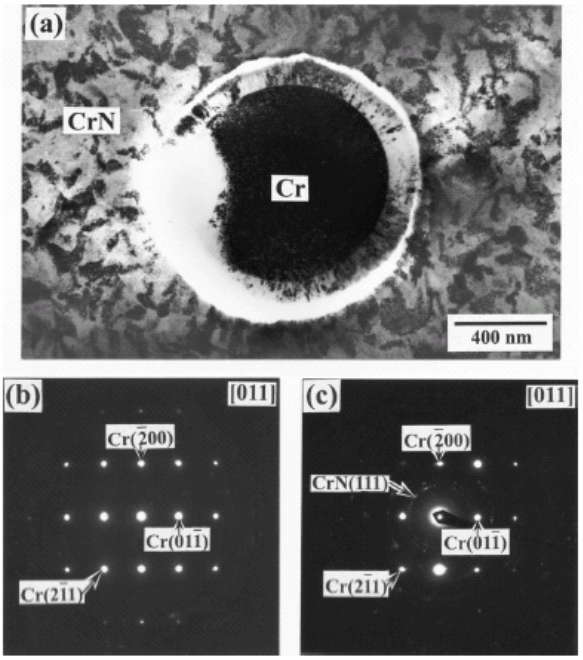

Figure 5. (a) Plan-view TEM micrograph of a macroparticle inlaid in a CrN coating. Selected area diffraction patterns of (b) the central Cr grain and (c) the outer CrN shell of the macroparticle.

(1670°C) within 200 mm from the cathode and hence solidified. When the radius was larger than 2 μm, the droplets remained in the liquid state and had a flat-bottomed geometry after deposition on the substrate. Keidar *et al.*[17] reported that the temperature of Ti droplets with a radius of 0.1 μm, deposited at different plasma densities, dropped rapidly from 1726 to 1100°C within 10^{-4} s on emission from the cathode, *i.e.*, transforming from liquid state to solid state. Accordingly small Cr droplets emitted from the cathode solidified during their travel to the substrate, and reactions of the ionized metal and nitrogen formed a thin nitride layer on the surface of the droplets. In addition, Keidar *et al.*[17] pointed out that the surface energy was higher than the kinetic energy for a small droplet. This suggests that the shape of small droplets remained spherical, but for the larger

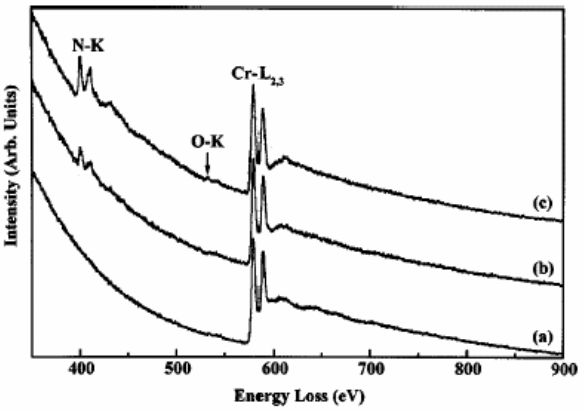

Figure 6. The EELS spectra of (a) the central Cr grain, (b) the inner, and (c) the outer portions of the CrN shell in the macroparticle of Fig. 4a.

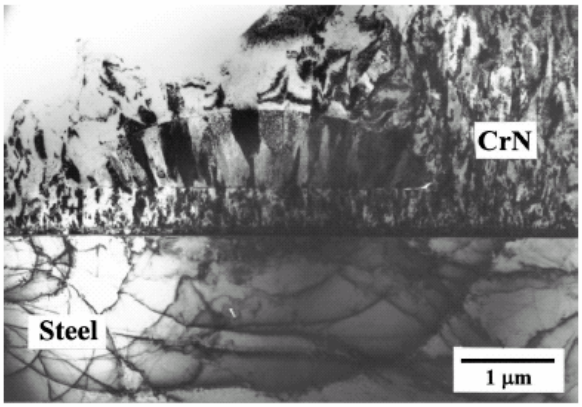

Figure 7. Large semielliptical-shaped Cr droplet is embedded in the CrN coating.

ones the surface energy alone is not enough to maintain the spherical shape when the droplets collide with the substrate and they became flat-bottomed droplets, as shown in Fig. 7, where a semielliptical-shaped Cr droplet is present in the CrN coating. The diameter at the base of the droplet was 4 μm.

Once the macroparticle collides with the CrN coating and stays on the surface, voids beneath the macroparticle can form due to the shadowing effect of the ion flux. After a short time, the coating geometry of the macroparticle becomes eccentric, as shown in Fig. 9c. Subsequent growth of chromium nitrides on the macroparticle surface follows the orientation of the previously deposited CrN to form a radiated-type structure, until coalescence with the regular CrN columns perpendicular to the substrate surface occurs. The flattened toroidal void formed beneath the macroparticle within the CrN coating is sealed as the deposition continues; see Fig. 9d or Fig. 4. Similar TEM observations have been reported in previous studies of macroparticles in the TiN or TiAlN coatings.[1,9,10] Because the macroparticles are covered by a thick layer of CrN near the coating surface, can explain why the image contrast between the macroparticles and the surrounding nitride matrix is weak in the BEI mode of SEM observation.

The edges of the torus are inclined to the surface due to continuous growth of the macroparticle. The toroidal void, if present near the coating surface, weakens the adherence of the macroparticle to the coating.[18-20] Keidar *et al.*[19] suggested that electrical charges may accumulate on the metal droplets emitting from the cathode while passing through the plasma zone, and a repulsion force is likely to be developed between the macroparticles and a substrate that is also under negative bias, resulting in a weak bonding at the interface. Thus the protruded macroparticles are likely to be spalled off on cooling of the coated specimen to room temperature due to the difference in the coefficients of thermal expansion between the macroparticles and the nitride coating. As a result, pinholes are readily produced on the coating surface as shown in Fig. 8. The pinholes are known to be detrimental to the erosion and corrosion resistances of the coating.[20]

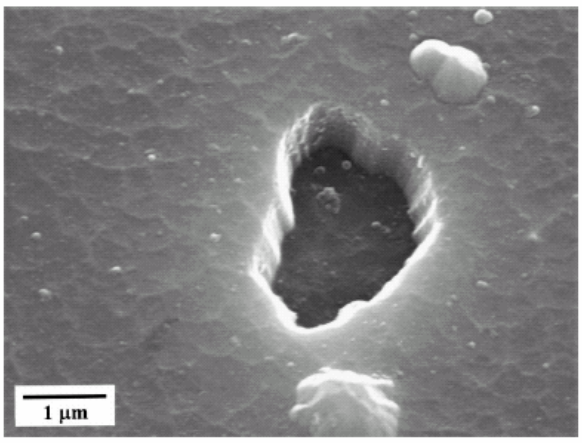

Figure 8. Pinhole left on the surface of the CrN coatings after macroparticles spalled off the coating.

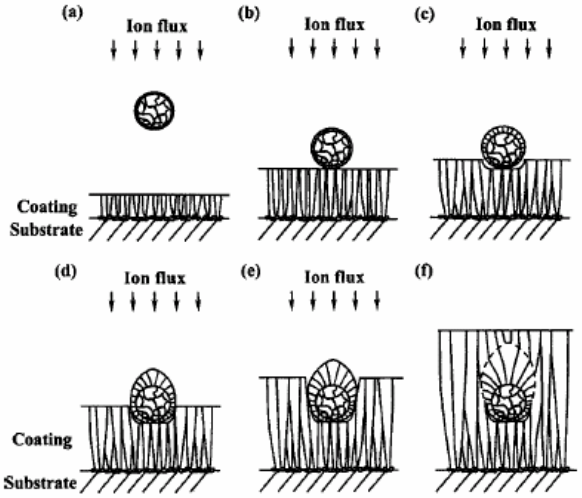

Figure 9. Schematic diagram showing the formation mechanism of a macroparticle and its surface morphology in an arc ion-plated CrN coating.

As deposition continues, the CrN coating keeps growing and produces a crater around the macroparticle as shown in Fig. 9e or Fig 2. If deposition of the CrN coating is stopped in situations like Fig. 9d or e, there will be a conical protrusion on the coating surface, resulting in rough surface morphology. Because the net growth rate of the CrN columns that are perpendicular to the substrate surface is higher than those inclined, *i.e.*, the CrN surrounding the macroparticle, dimples around the macroparticle are formed as seen in Fig. 2. If deposition continues, some of the macroparticles eventually may be embedded in the coating as depicted in Fig. 9f. Because the CrN coating located on top of the macroparticle has similar orientations to the coating matrix, the boundary between them is difficult to distinguish, as indicated by the dashed line in Fig. 9f.

In a previous study of the growth defects in arc-evaporated TiN coatings using conventional SEM by Aharonov *et al.*[1] the formation mechanism of conical features on the coating surface was proposed, which is in part similar to the current model. However, since the spatial resolution of the TEM and field emission SEM used in this study is much higher than that of the conventional SEM used by Aharonov *et al.*, new information regarding the microstructure of the macroparticles in arc-evaporated coatings has been obtained by this research. First, as shown in Fig. 4 the metal droplet is surrounded by a nonuniform nitride layer, not only near the coating surface due to subsequent deposition, but also on the opposite side, *i.e.*, near the bottom of the crater, implying that the core-shell structure of the metal droplet shown in Fig. 9a and b must be formed before it reaches the substrate. Second, toroidal voids exist under the macroparticles resulting from the shadowing effect of the ion flux during subsequent deposition, as can be seen in Fig. 4 and 7. Third, dimples, as shown in Fig. 2 and 3, are always present around the macroparticles on the coating surface due to a difference in the

growth rate of the CrN columns at different orientations.

Chemical analysis of the CrN macroparticles.—EELS has very good sensitivity for light-element detection compared with X-ray microanalysis,[21] and is well suited for detecting elements such as nitrogen and oxygen in the macroparticles. In this study, the EELS analysis of the CrN macroparticles was done on the plan-view TEM specimen shown in Fig. 5. Figure 6 gives a series of EELS spectra from the central Cr droplet toward the outer shell CrN of the macroparticle. In the spectrum of the central Cr droplet in Fig. 6a, a small peak corresponding to the K edge of oxygen is barely seen in front of the L edges of Cr. On background subtraction using exponential curve fitting,[21] the oxygen content in the central Cr is calculated to be 4.6 atom %. Figures 6b and c are the EELS spectra taken from the inner and outer portions of the surrounding CrN shell. The peak corresponding to the K edge of nitrogen shows up clearly in Fig. 6b and the content of nitrogen increases slightly in Fig. 6c. Quantitative analysis of these spectra indicates that the nitrogen and oxygen concentrations in the CrN coating surrounding the macroparticle increase from 17.7 to 38 atom % and 7.7 to 9.5 atom %, respectively, in Fig. 6b and c. Compared with the EELS results of TiN macroparticle in a previous report,[9] the concentration of oxygen in the TiN macroparticles is much higher, up to 25.5 atom %, than that in the CrN macroparticles. The result can be understood from thermodynamics in that the affinity of oxygen with Ti is higher than that with Cr,[22] although, strictly, the system is not necessarily under equilibrium. In addition, the only chromium nitride phase that was identified in the SAD pattern of Fig. 5c is CrN, unlike the TiN macroparticles, in which the outer shell of the macroparticles was composed of the $TiN_{0.26}$, α-$TiN_{0.3}$, Ti_2N, and TiN phases.[9]

Conclusions

Macroparticles in arc ion-plated CrN coatings have been characterized by energy filtering TEM and SEM. The macroparticles in the arc ion-plated coatings have a core-shell microstructure and a bud shape. The core region consists of metallic Cr while the outer shell contains only the CrN phase. A formation mechanism of the macroparticles produced by arc evaporation deposition is proposed based on the analytical results. This model explains the weak image contrast present between the macroparticles protruding the surface and their surrounding nitride matrix during SEM observation using X-ray mapping and/or backscattered electron imaging.

Acknowledgments

Financial support of this research by the National Science Council of Taiwan under contract no. NSC 90-2216-E-005-022 is acknowledged. The assistance of SEM operation by T. N. Lin and Professor J. P. Chu at National Taiwan Ocean University is also gratefully appreciated.

National Chung Hsing University assisted in meeting the publication costs of this article.

References

1. R. R. Aharonov, M. Chhowalla, S. Dhar, and R. P. Fontana, *Surf. Coat. Technol.*, **82**, 334 (1996).
2. A. W. Baouchi and A. J. Perry, *Surf. Coat. Technol.*, **49**, 253 (1991).
3. J. Kourtev, R. Pascova, and E. Weißmantel, *Thin Solid Films*, **287**, 202 (1996).
4. P. J. Martin, R. P. Netterfield, and T. J. Kinder, *Surf. Coat. Technol.*, **49**, 239 (1991).
5. M. Hakovirta, V. M. Tiainen, and P. Pekko, *Diamond Relat. Mater.*, **8**, 1183 (1999).
6. I. I. Beilis, M. Keidar, R. L. Boxman, and S. Goldsmith, *Surf. Coat. Technol.*, **108-109**, 148 (1998).
7. R. L. Boxman and S. Goldsmith, *J. Appl. Phys.*, **52**, 151 (1981).
8. Z. Cheng, M. Wang, and J. Zou, *Surf. Coat. Technol.*, **92**, 50 (1997).
9. M. H. Shiao and F. S. Shieu, *Thin Solid Films*, **386**, 27 (2001).
10. M. H. Shiao and F. S. Shieu, *J. Vac. Sci. Technol.* **19**, 703 (2001).
11. R. L. Boxman and S. Goldsmith, *Surf. Coat. Technol.*, **52**, 39 (1992).
12. J. E. Daalder, *J. Phys. D*, **9**, 2379 (1976).
13. T. Utsumi and J. H. English, *J. Appl. Phys.*, **46**, 126 (1975).
14. P. J. Martin, D. R. Mckenzie, R. P. Netterfield, P. Swift, S. W. Filipczuk, K. H. Müller, C. G. Pacey, and B. James, *Thin Solid Films*, **153**, 91 (1987).
15. T. B. Massalski, H. Okamoto, P. R. Subramanian, and L. Kacprzak, *Binary Alloy Phase Diagrams*, ASM, Materials Park, OH (1990).
16. S. Anders, A. Anders, K. M. Yu, X. Y. Yao, and I. G. Brown, *IEEE Trans. Plasma Sci.*, **21**, 440 (1993).
17. M. Keidar, I. Beilis, R. L. Boxman, and S. Goldsmith, *Surf. Coat. Technol.*, **86-87**, 415 (1996).
18. H. Ljungcrantz, L. Hultman, J. E. Sundgren, G. Håkansson, and L. Karlosson, *Surf. Coat. Technol.*, **63**, 123 (1994).
19. M. Keidar, I. Beilis, R. L. Boxman, and S. Goldsmith, *IEEE Trans. Plasma Sci.*, **23**, 902 (1995).
20. M. Nishibori, *Surf. Coat. Technol.*, **52**, 229 (1992).
21. R. F. Egerton, *Electron Energy Loss Spectroscopy in Electron Microscopy*, Plenum Press, New York (1996).
22. *Metals Handbook*, 9th ed., Vol. 3, ASM, Metals Park, OH (1979).

Available online at www.sciencedirect.com
SCIENCE DIRECT®
Thin Solid Films 436 (2003) 238–243
thin solid films
www.elsevier.com/locate/tsf

Effect of metal vapor vacuum arc Cr-implanted interlayers on the microstructure of CrN film on silicon

Sheng Han[b], Hong-Ying Chen[c], Zue-Chin Chang[c], Jian-Hong Lin[a], Ching-Jung Yang[c], Fu-Hsing Lu[c], Fuh-Sheng Shieu[c], Han C. Shih[a,c,*]

[a]*Department of Materials Science and Engineering, National Tsing Hua University, 101 Kuang Fu Rd., Sec. 2, Hsinchu, Taiwan 300, ROC*
[b]*National Taichung Institute of Technology, 129 San-Min Rd., Sec. 3, Taichung, Taiwan 404, ROC*
[c]*Department of Materials Engineering, National Chung Hsing University, 250 Kuo Kuang Rd., Taichung, Taiwan 402, ROC*

Received 10 July 2002; received in revised form 27 February 2003; accepted 25 March 2003

Abstract

The effect of metal vapor vacuum arc (MEVVA) Cr-implanted interlayers on the microstructure of CrN films on the silicon wafer was investigated. Two types of the CrN-coated specimens (CrN/Si and CrN/Cr/Si) by cathodic arc plasma deposition were prepared with and without a MEVVA Cr-implanted interlayer. The diffraction patterns of the coated specimens revealed the presence of CrN, and the (220) preferred orientation for both CrN/Si and CrN/CrN/Si. The CrN coating thicknesses for CrN/Si and for CrN/Cr/Si were 0.3 μm and 1.3 μm, respectively. Secondary ion mass spectrometry proved the high quality of the films on silicon substrates. Transmission electron microscopy micrographs and selective area diffractions revealed the presence of a large number of nano-scale Cr resulting from the interlayer of MEVVA Cr with a background of single crystal silicon spots. Furthermore, in situ stress measurement demonstrated that the presence of a Cr interlayer between CrN and Si could drastically reduce the residual stress in the CrN/Cr/Si assembly.

Keywords: Metal vapor vacuum arc; Secondary ion mass spectrometry; Transmission electron microscopy; Residual stress

1. Introduction

Chromium nitride (CrN) films have been successfully applied in tools because of their excellent mechanical properties and corrosion resistance [1–3]. In our previous studies, a Cr interlayer was electroplated to increase the corrosion and tribological resistance of CrN films [1]. However, the electroplating industry is notorious for its pollution of the environment and the residual stress in this material system interlayer has seldom been investigated. Thus, this study employed metal vapor vacuum arc (MEVVA) ion implantation to deposit an interlayer of Cr. This method has many outstanding advantages, such as the ability to produce almost all species of metal ion, a very high current, pure ion beams, reasonably high charge states and a large beam spot [4]. This technique also allows the use of cathodic arc plasma deposition (CAPD) for forming CrN [5], and this study employs silicon wafers as the substrate. Two specimens were prepared; one was a pre-coated interlayer of Cr between the CrN film and the Si substrate, designated as CrN/Cr/Si and the other was CrN directly deposited on the Si substrate, designated as CrN/Si. The in situ residual stress measurements [6] were made to investigate the effect of an interlayer Cr on the residual stress. Understanding the effect of residual stress is useful in further studies.

2. Experimental details

A 725 μm thick p-type (100) Si wafer (Toshiba Ceramics Co., Ltd.) was selected as a substrate. The Cr interlayer was deposited using an MEVVA ion implanter at an extracting voltage of 50 kV. Nevertheless, the extracted Cr ions have various valencies, including Cr^{+}, Cr^{2+}, Cr^{3+} and Cr^{+4} [7]. The main component

*Corresponding author: Tel.: +886-3-571-5131 ext. 3845; fax: +886-3-571-0290.
E-mail address: hcshih@mse.nthu.edu.tw (H.C. Shih).

0040-6090/03/$ - see front matter © 2003 Elsevier Science B.V. All rights reserved.
PII: S0040-6090(03)00600-X

was Cr^{2+} with a corresponding average energy of 100 keV. The ion doses and the current density were 2×10^{17} ions/cm^2 and 6 μA/cm^2, respectively. The substrate temperature was measured by K-type thermocouples and the substrate was heated from nominal room temperature up to approximately 100 °C after implantation. A CAPD technique was used to produce CrN films. During the deposition, the substrate temperature was maintained at ~350 °C at a bias of −150 V; the arc current was 60 A; the N_2 partial pressure was controlled at ~3 Pa, and the deposition time was 70 min.

The crystal structures of CrN/Si and CrN/Cr/Si assemblies were investigated by X-ray diffraction (XRD) and transmission electron microscopy (TEM). A Mac Science MXP3 diffractometer using Cu K_α radiation ($\lambda=0.154$ nm) with the collected interval of $0.02°/2\theta$ was used. A Philips CM2 TEM operating at 200 kV was used to examine the crystal structure of the Cr/Si assembly. The surface morphology and the thickness were measured by scanning electron microscopy (SEM), JEOL JSM-5400, operating at 15 kV. A Cameca IMS-4F secondary ion mass spectrometer (SIMS) with a Cs^+ primary beam with an impact energy of 14.5 keV and a primary current of 50 nA traced the depth profiles of chromium, nitrogen and silicon in the films. In situ curvature measurements were made using a scanning laser curvature method to determine the stress changes in the film. A He–Ne laser with a wavelength of 632.8 nm and a power of 7 mW was used. The laser spot was approximately 0.25 cm and moved through 1 cm on the surface of specimen. The curvature ($1/R$) of the film was obtained and the residual stress (σ_f) calculated using the Stoney's equation [8]:

$$\sigma_f=\frac{E_S}{6(1-\nu_S)}\times\frac{t_S^2}{t_f}\times\left(\frac{1}{R}\right) \quad (1)$$

where ν_S is the Poisson ratio of the substrate; E_S is Young's modulus of the substrate; t_f is the thickness of the film, and t_S the thickness of the substrate.

3. Results and discussion

3.1. XRD results

Firstly, XRD was used to examine the crystal structure of CrN/Si and of CrN/Cr/Si assemblies, as shown in Fig. 1. The two assemblies match the CrN phase as given in the JCPDS card [9]. Notably, the 2θ value of 33.01° is attributed to the second reflection from the Si substrate. The (200) and (220) diffraction line of the CrN phase is observed for both samples. Furthermore, the predominance of CrN (220) is the preferred orientation after the JCPDS card is compared with [9]. Such an obtained (220) orientation has a slightly lower

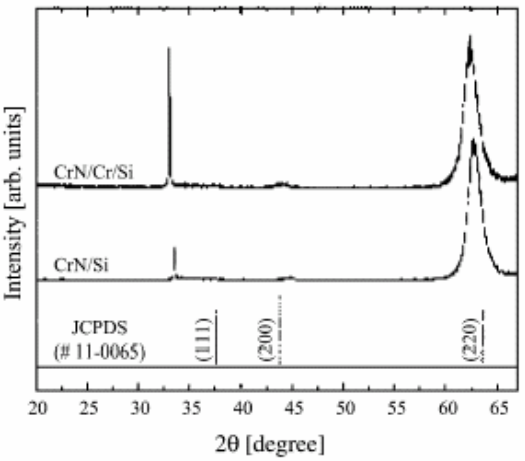

Fig. 1. XRD patterns of CrN/Si and CrN/Cr/Si showing a pronounced preferred orientation of (220).

diffraction angle, indicating a compressive residual stress in the film, which deserves to be examined further using a scanning laser curvature measurement. The full width at half maximum (FWHM) of the diffraction peak normally represents the grain size in Scherrer's equation. The grain sizes of the CrN/Si and CrN/Cr/Si assemblies are similar because of the similarity of the two FWHMs (1.47 vs. 1.74). The Cr interlayer does not affect the preferred orientation of the CrN films; this fact is consistent with the authors' previous studies on electroplated Cr as an interlayer [5].

3.2. SEM observation

Fig. 2 presents the SEM morphologies of the scattering of macroparticles on the surface films of the CrN/Si and CrN/Cr/Si assemblies. Macroparticles may result from the reactive force of intensive ions that flow back from the ionization region onto the underlying liquid pool of the chromium target, or from the plasma-generated micro-explosions on the cathode surface [10]. The macroparticles revealed by EDS consist of pure chromium. Fig. 2a,b depicts the decohesion of macroparticles at the particle-matrix interface while Fig. 2c,d shows the cross-sectional morphologies of the CrN/Si and CrN/Cr/Si assemblies. The surface morphologies are essentially the same and independent of the Cr interlayer. However, the difference in CrN film thickness, 0.3 μm for CrN/Si and 1.3 μm for CrN/Cr/Si, can be explained by the fact that the Cr ions implanted interlayer facilitates the nucleation and growth of CrN, which result in contrast to the results of our previous studies on the use of electroplated Cr to bridge the succeeding CrN coating resulting in well-textured forms [5].

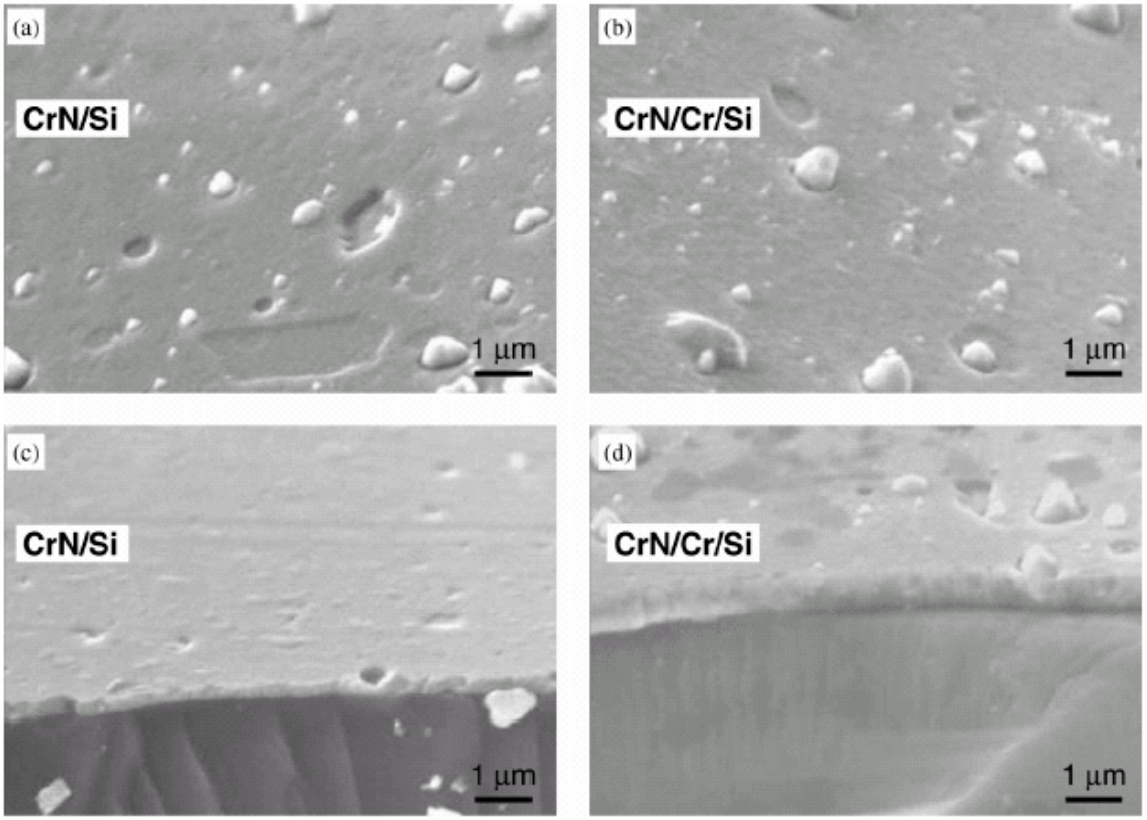

Fig. 2. SEM surface morphology of the films: (a) CrN/Si; and (b) CrN/Cr/Si and the corresponding SEM cross sectional morphology of the films: (c) CrN/Si; and (d) CrN/Cr/Si.

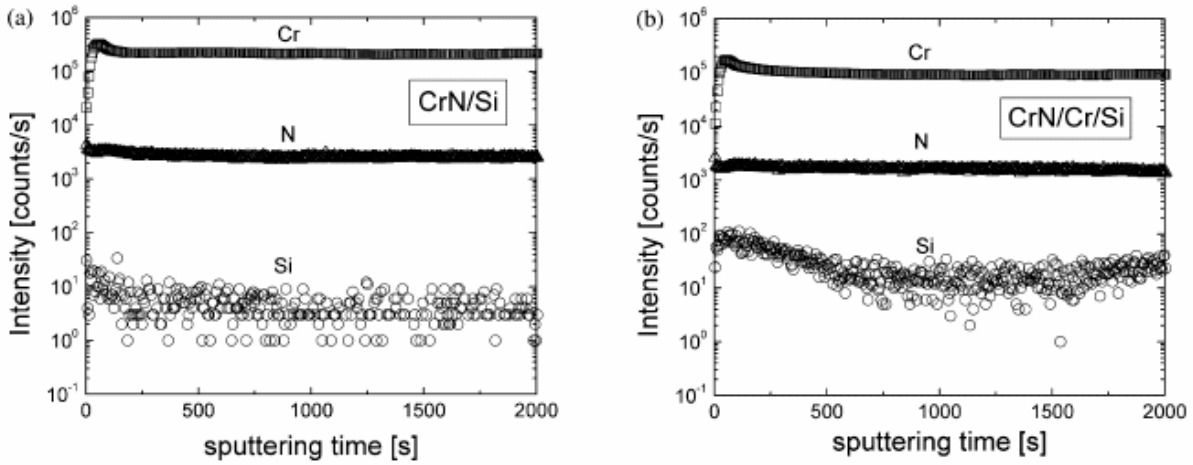

Fig. 3. The depth profile of elemental Cr, N, and Si as a function of sputtering time for (a) CrN/Si and (b) CrN/Cr/Si.

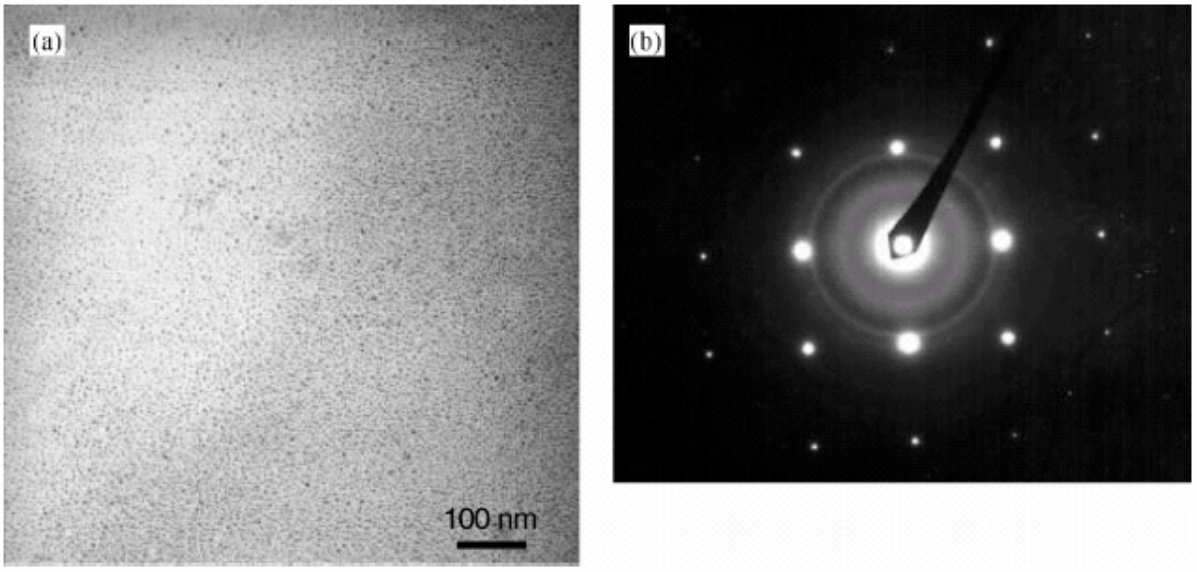

Fig. 4. (a) TEM micrograph of the MEVVA Cr deposited silicon showing the presence of a larger number of nano-scale Cr and (b) SAD pattern resulting from the MEVVA Cr deposited silicon showing diffraction rings on a background of single crystal silicon spots.

3.3. SIMS analysis

SIMS was conducted to elucidate the elemental distribution of chromium and nitrogen in the CrN films for CrN/Cr/Si and for CrN/Si assemblies. Fig. 3a,b shows the logarithmic intensities associated with chromium and nitrogen with silicon noise as a function of sputtering time for CrN/Si and CrN/Cr/Si assemblies, respectively: good quality films on the silicon substrates are observed. For instance, the acquired homogeneity is exhibited in the depth of the layers, showing similar intensity variations for CrN/Si and CrN/Cr/Si. The stoichiometric ratio of nitrogen and chromium in the CrN film cannot be changed significantly by the MEVVA Cr ion-implanted interlayer, as resolved from the SIMS depth profiles.

3.4. TEM observation

TEM was used to disclose the microstructure of the Cr interlayer by MEVVA. Fig. 4a,b shows the plan-view bright field image and selected area diffraction (SAD) pattern of the MEVVA Cr-deposited silicon wafer, respectively, implying the presence of a large number of nano-clusters (Fig. 4a) and a weak diffraction pattern (Fig. 4b) with a background of single crystal silicon spots, associated with the thin MEVVA Cr interlayer. The d-spacing calculated for the diffraction rings matches with the standard d-value of Cr [11]. The presence of such Cr diffraction rings proves that chromium disilicide ($CrSi_2$) was not formed here.

$CrSi_2$ can be directly synthesized using MEVVA techniques at a substrate temperature of 150 °C and a current density $\geqq 8.8\ \mu A/cm^2$ [7,12]. Nevertheless, both the current density ($6\ \mu A/cm^2$) and the substrate temperature (approx. 100 °C) used in the performed experiment are consistently lower than required, seemingly explaining why $CrSi_2$ could not be produced.

Although $CrSi_2$ can be synthesized by solid–state diffusion (thermal annealing) [13,14], no such phase could be detected after CrN was deposited by CAPD. The substrate temperature was ~350 °C while the CrN film were being deposited, so insufficient energy was provided for Cr atoms to react further with the Si substrate.

3.5. Residual stress analysis

The residual stresses of the CrN/Si and CrN/Cr/Si assemblies and the differences between them were evaluated and compared. Residual stress often exists in deposited films and originates from two major sources: one is the intrinsic stress that depends on a deposition parameter such as, ion bombardment energy and the other is the thermal stress that is caused by the different thermal expansion coefficients between the film and the substrate [15–18]. The residual stresses were determined experimentally by a scanning laser curvature method, and the curvature was further converted into stress using Eq. (1). The needed parameters are, $E_S = 130.2$ GPa, $\nu_S = 0.279$ [19], $t_S = 725\ \mu m$ and t_f is the corresponding thickness of the CrN film observed by SEM, 0.3 μm

Table 1
A comparison between CrN/Si and CrN/Cr/Si assemblies determined by XRD, SEM and in situ stress measurements

Specimens	Preferred orientation	CrN films thickness (μm)	Measured curvature (m^{-1})	Residual stress (GPa)
CrN/Si	CrN (220)	0.3	-0.16 ± 0.01	-8.02 ± 0.53
CrN/Cr/Si	CrN (220)	1.3	-0.24 ± 0.01	-2.77 ± 0.12

for CrN/Si and 1.3 μm for CrN/Cr/Si. The residual stresses for CrN/Si and for CrN/ Cr/Si are −8.0 GPa and −2.8 GPa, respectively, as shown in Table 1. The obtained stress levels are reasonable in comparison with the values in the literature (−2.9 to −8.8 GPa) [2,6,20,21].

The thermal stress of CrN (σ_{CrN}) can be estimated as follows [22]

$$\sigma_{CrN}=\frac{(\alpha_{CrN}-\alpha_{Si})\Delta T}{\left[\frac{\nu_{crN}-1}{E_{CrN}}+\frac{h_{CrN}(\nu_{CrN}-1)}{h_{Si}E_{Si}}\right]} \quad (2)$$

where α is the thermal expansion coefficient ($\alpha_{CrN}=2.3\times10^{-6}$ K^{-1}, $\alpha_{Si}=4.1\times10^{-6}$ K^{-1}); ν is the Poisson's ratio ($\nu_{CrN}=0.199$, $\nu_{Si}=0.279$); E is Young's modulus ($E_{CrN}=452$ GPa, $E_{Si}=130.2$ GPa); h is the thickness of the films and substrates, and ΔT is the difference between the deposition temperature and the room temperature. The thermal stress (σ_{CrN}) is only 0.3 GPa for depositing CrN deposition herein, contributing approximately 4% for CrN/Si and 12% for CrN/Cr/Si. Therefore, the residual stress is mainly the intrinsic stress.

Surprisingly, an MEVVA Cr interlayer can drastically reduce the residual stress in the CrN film. To estimate the magnitude of the reduction of stress, the reduction of stress $\Delta\sigma$ can be defined as,

$$\Delta\sigma=|(\sigma_{CrN/Cr}-\sigma_{CrN})/\sigma_{CrN}|\times100\% \quad (3)$$

where $\sigma_{CrN/Cr}$ and σ_{CrN} are the corresponding residual stress with and without the MEVVA Cr interlayer, respectively. The role of the Cr interlayer is apparent: it can significantly relax the residual stress of CrN films by up to 65%. It can therefore effectively reduce the residual stress in the growing of CrN films, using Eq. (3).

4. Conclusions

This study compared and characterized the microstructures and residual stress of CrN on a silicon wafer formed by CAPD both with and without a Cr intermediate layer deposited by MEVVA using XRD, SEM, TEM and SIMS.

1. No intermediate phases of $CrSi_2$ were formed between the MEVVA Cr and the Si substrate after MEVVA Cr implantation and subsequent CrN coating.
2. The diffraction patterns of the specimens indicated the presence of the CrN phase, with a (220) preferred orientation for both CrN/Si and CrN/CrN/Si.
3. The plan-view bright field TEM and its SAD reveal the presence of a large number of nano-clusters and a diffraction pattern with a background of single crystal silicon spots from the interlayer of MEVVA Cr.
4. The origin of the diffraction ring is a clear indication of the nano-crystalline Cr deposited by MEVVA.
5. Moreover, in situ stress measurements demonstrate that the presence of a Cr interlayer between CrN and Si can dramatically reduce the residual stress in CrN films.

Acknowledgments

The authors would like to thank the National Science Council of the Republic of China, for financially supporting this research under contract number of NSC 91PFA0400049. The Surftech Corporation, Taiwan is also highly appreciated for preparing the MEVVA Cr and CAPD CrN films. The authors would also like to thank Mr S.-S. Guo for his assistance in measuring the residual stresses.

References

[1] S. Han, J.H. Lin, S.H. Tsai, S.C. Chung, D.Y. Wang, F.H. Lu, H.C. Shih, Surf. Coat. Technol. 133–134 (2000) 460.
[2] M. Odén, C. Ericsson, G. Håkansson, H. Ljungcrantz, Surf. Coat. Technol. 114 (1999) 39.
[3] F.D. Lai, J.K. Wu, Surf. Coat. Technol. 88 (1996) 183.
[4] G. Brown, A. Anders, S. Anders, M.R. Dickinson, R.A. MacGill, E.M. Oks, Surf. Coat. Technol. 84 (1996) 550.
[5] S. Han, J.H. Lin, X.J. Guo, S.H. Tsai, Y.O. Su, J.H. Huang, F.-H. Lu, H.C. Shih, Thin Solid Films 377–378 (2000) 578.
[6] F.-H. Lu, H.-Y. Chen, Thin Solid Films 398–399 (2001) 368.
[7] H.N. Zhu, B.X. Liu, Appl. Surf. Sci. 161 (2000) 240.
[8] G.G. Stoney, Proc. R. Soc. Lond. Ser. A 82 (1909) 172.
[9] Powder Diffraction File, Joint Committee on Powder Diffraction Standard, ASTM, Philadelphia, PA, 1996, Card 11-0065.
[10] R.L. Boxman, S. Goldsmith, Surf. Coat. Technol. 57 (1992) 39.
[11] Powder Diffraction File, Joint Committee on Powder Diffraction Standard, ASTM, Philadelphia, PA, 1996, Card 06-0694.
[12] S. Wang, H. Liang, P. Zhu, Appl. Surf. Sci. 153 (2000) 108.
[13] J.O. Olowoafe, M.-A. Nicolet, J.W. Mayer, J. Appl. Phys. 47 (1976) 5182.

[14] E.G. Colgan, B.Y. Tsaur, J.W. Mayer, Appl. Phys. Lett. 37 (1980) 938.
[15] H. Windischmann, J. Vac. Sci. Technol. A9 (1991) 2431.
[16] J.A. Sue, A.J. Perry, J. Vetter, Surf. Coat. Technol. 68/69 (1994) 126.
[17] H. Oettel, R. Wiedemann, Surf. Coat. Technol. 76–77 (1995) 265.
[18] T. Matsue, T. Hanabusa, Y. Ikeuchi, Thin Solid Films 281–282 (1996) 344.
[19] W.A. Brantly, J. Appl. Phys. 44 (1973) 534.
[20] M.C. Bost, J.E. Mahan, J. Appl. Phys. 63 (1988) 839.
[21] W. Herr, E. Broszeit, Surf. Coat. Technol. 97 (1997) 335.
[22] W.D. Kingery, H.K. Bowen, D.R. Uhlmann, Introduction to Ceramics, John and Wiley, New York, NY, 1976, pp. 197–199.

ELSEVIER

Intermetallics 8 (2000) 623–627

Intermetallics

Microstructure and shear strength of a Au–In microjoint

F.S. Shieu *, Z.C. Chang, J.G. Sheen, C.F. Chen

Institute of Materials Engineering, National Chung Hsing University, Taichung 402, Taiwan

Abstract

Two types of Au–In microjoints, i.e. Au/In/Au in which In foil was used and Au/In, were prepared by either solid state interdiffusion (SSID) or solid–liquid interdiffusion (SLID) bonding for single lap tensile test. Deposition of the Au and In thin films was carried out by thermal evaporation on a polyethylene terephthalate (PET) substrate. It is found that the shear strength of the Au/In microjoints is higher than that of Au/In/Au using In foil. It is also observed that the fracture mode of Au–In microjoints depends on the types of In used. Failure of the Au/In microjoints appeared to be along the joint–substrate interface, whereas it occurred within the In foil for the other type of specimens. Examination of the Au/In microjoints by glancing angle X-ray diffraction reveals the presence of the two major constituent phases, Au_7In_3 and Au, as well as other intermetallics $AuIn_2$, $Au_{10}In_3$, and Au_9In_4 in small amount. On the other hand, only the intermetallic $AuIn_2$ and pure In were observed in the Au/In/Au microjoints, where the total thickness of In is much higher than that of Au.

Keywords: D. Microstructure; F. Electron microscopy, transmission; F. Diffraction

1. Introduction

Indium (In)-containing alloy solders show a longer fatigue life, better mechanical properties and reliability than conventional tin (Sn)-containing alloys as solder interconnections for electronic packaging [1–4]. As a result, indium and its alloys are considered to be used in the surface mount technology for various microelectronic devices in the future. From the processing point of view, indium has lower melting point, 156°C, than that of tin, 232°C, thus the joining temperature can be reduced further. To take advantage of this merit and also improve the service life of a In-containing microjoint, a new bonding technique, called solid-liquid interdiffusion bonding (SLID) [5,6], has recently been introduced in electronic packaging industry.

The SLID process uses a multilayer of high-melting and low-melting materials as a bonding preform and is carried out at temperatures above the melting point of the low-melting material. Subsequently metallurgical transformation takes place between the high- and low-melting materials and the low-melting material is gradually consumed, resulting in a microjoint which contains only intermetallics and/or the high-melting material. By properly controlling the film thickness and processing conditions, it is possible to form a strong microjoint free from the low-melting material. This technology will allow the system designers of electronic packaging to reverse the conventional soldering hierarchy of lower and lower process temperatures of subsequent manufacturing steps.

Since the technology relies on the formation of an intermetallic, it is important to understand the phase formation during joining and its influence on the mechanical properties of the microjoints as well. In this study, both transmission electron microscopy and glancing angle X-ray diffraction are used to study the microstructure and phase formation of the Au–In microjoints. In addition, the effect of In thickness on the shear strength of the microjoints is presented and discussed.

2. Experimental

Two types of Au–In microjoints, i.e. Au/In/Au and Au/In, schematically shown in Fig. 1, were prepared, in which the former contains an In foil of 20 μm thick, while the latter uses an In thin film of 2 μm thick. Specimens containing the In foil were made by depositing a thin layer of Au about 5 μm thick, using thermal evaporation, on a polyethylene terephthalate (PET) substrate of dimensions 5×10×0.2 mm for use in a single lap tensile test. The base pressure for Au evaporation was 8×10^{-6} torr and rised up to 2×10^{-5} torr during deposition. The In foil was then sandwiched between

* Corresponding author. Tel.: +886-4-285-4563; fax: +886-4-285-7017.

E-mail address: fsshieu@dragon.nchu.edu.tw (F.S. Shieu).

0966-9795/00/$ - see front matter
PII: S0966-9795(99)00147-8

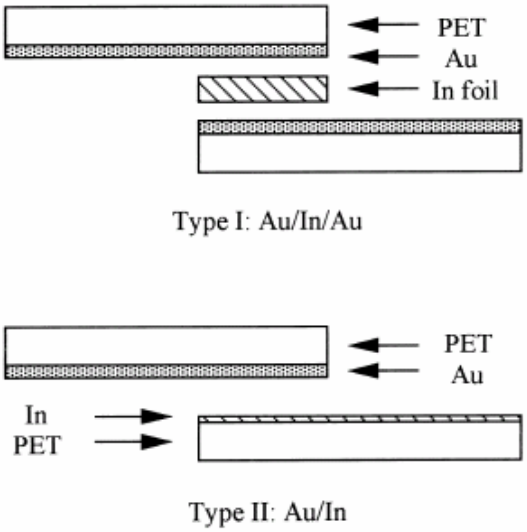

Fig. 1. Schematic of the two types of specimen geometry for single lap tensile test.

two Au-coated PETs and joining was carried out in air at 250°C for 5 min. The other type of specimens was produced by hot pressing the Au-coated PET with an In-coated PET together in air at temperatures spanning from 100 up to 250°C and duration from 1 to 30 min (see Table 1). The In thin films were prepared also by thermal evaporation and the chamber pressure was maintained at 5×10^{-4} torr during deposition.

The shear strength of the Au–In microjoints was evaluated by single lap tensile test. The fracture morphology of the tested specimens was examined by a JEOL 5400 scanning electron microscope operated at 20 KeV. Intermetallic phase formation within the microjoints was investigated by glancing angle X-ray diffraction using Cu K_α radiation with incident angle fixed at three different values 0.1°, 0.5° and 1.0°.

Microstructure of the microjoints was characterized by a Zeiss 902A energy filtering transmission electron microscope (TEM) operated at 80 KeV. Thin sections about 100 nm thick were made by a Reichert Ultracut E ultramicrotome for TEM observation.

3. Results and discussion

3.1. Shear strength of the Au–In microjoints

A single lap joint loaded in tension is the most common test geometry for evaluating adhesive joints. If the stress concentrations arising from the differential straining of the bonded substrates and from the eccentricity of the loading path can be neglected, the ultimate shear stress, τ_{uss}, of the adhesive joint is related to the applied tensile load, F, by $\tau_{uss} = F/A$, where A is the bonded area.

The test result of the Au–In microjoints produced using different geometry and under different joining conditions is given in Table 1, in which has been included the shear strength of pure In and the PET substrate. It is found that on the average the Au/In microjoints exhibit higher shear strength than those of Au/In/Au which contain In foil. The shear strength of the Au/In microjoints prepared below the melting point of In, which undergo solid state interdiffusion, and above the melting point of In, which undergo solid–liquid interdiffusion, is quite similar. It is also noted that the duration of hot pressing shows insignificant effect on the measured shear strength. Nevertheless, the shear strength of the Au/In/Au microjoints is apparently higher than that of the pure In, likely due to a difference in the defects content in the In [6]. Fig. 2 shows the fracture surface of the In foil in a Au/In/Au microjoint in which failure of the single lap specimen occurred within the In. Cavities and stretching in the In due to shear deformation can be easily observed.

The most striking outcome of the mechanical test is the change of failure modes in the microjoints with the types of In used for joining. It is obtained that failure of the single lap specimens containing In foil occurred within the In layer, whereas it took place at either the Au–PET or the In–PET interfaces when In thin films

Table 1
The processing conditions, measured shear strength and observed phases in the Au–In microjoints

Types of specimen geometry	Hot pressing conditions		Shear strength (MPa)	Observed phases	Remarks
	Temp (°C)	Time (min)			
I	250	5	1.0 ± 0.14	In, $AuIn_2$	SLID bonding
II	250	1~5	1.5 ± 0.51	Au_7In_3, Au_9In_4, Au	SLID bonding
	200	5~30	1.13 ± 0.19	Au_7In_3, Au_9In_4, Au,	
	150	5~30	1.25 ± 0.50	Au_7In_3, $AuIn_2$, Au,	SSID bonding
	100	5~30	1.13 ± 0.64	Au_7In_3, $AuIn_2$, $Au_{10}In_3$, Au	
In			0.8 ± 0.10		Foil
PET			3.2 ± 0.18		Sheet

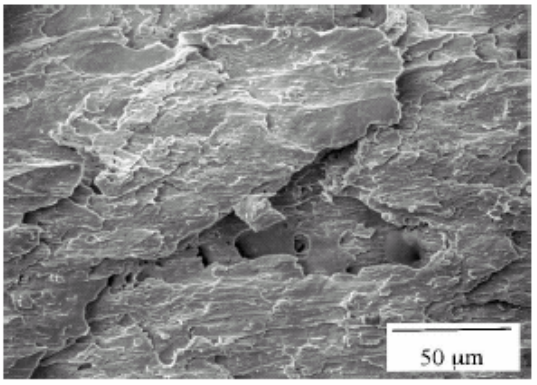

Fig. 2. A SEM micrograph of the fracture surface of a Au/In/Au microjoint where failure occurred within the In.

were used. Since the result of X-ray diffraction (see below) indicates that the thin film In was nearly consumed, only intermetallic phases and some remnant Au would be left in the microjoints. The shear strength of both Au and the various Au–In intermetallic compounds is expected to be higher than that of pure In, as reflected from the melting point of the phases [8]. As a result, phase transformation, via interdiffusion, of the low-melting In and high-melting Au into the various Au–In intermetallics has resulted in a strong Au–In microjoint. The real strength of the Au/In microjoints is, however, not known due to poor joint–substrate adhesion.

3.2. Analysis of the phase formation by X-ray diffraction

The result of single lap tensile test demonstrates the importance of layer thickness, which will eventually determine the phases formed upon joining, on the shear strength of Au–In microjoints. Typical X-ray spectra of a Au/In microjoint hot-pressed at 100°C for 15 min, in which delamination of the microjoint occurred along the In–PET interface are shown in Fig. 3. In addition to the peaks from PET and clay, both of which were used as an internal standard, intermetallic phases Au_7In_3, $AuIn_2$, and $Au_{10}In_3$, and pure Au are observed. The intensity of the Au (111) peak increases with the incident angle due to an increased X-ray interaction volume at higher incident angle. It is clear from the X-ray diffraction that the low-melting constituent In has been completely consumed and reacted with Au to form a variety of intermetallic phases after joining; thus a strong Au/In microjoint free from pure In is obtained. The depletion of In in the Au/In microjoint is also reflected in the color change of the In layer from bright to dark gray before and after joining, while viewing through the transparent PET substrate.

A summary of X-ray diffraction result of the various specimens prepared for the single lap tensile test is given in Table 1. From the table it can be seen that Au_7In_3 and Au are the common phases observed in all the Au/In microjoints, and indeed they are the two major constituent phases detected in the X-ray spectra. This can be rationalized by the fact that the atomic composition of Au_7In_3 is close to the thickness ratio of Au (5 μm)

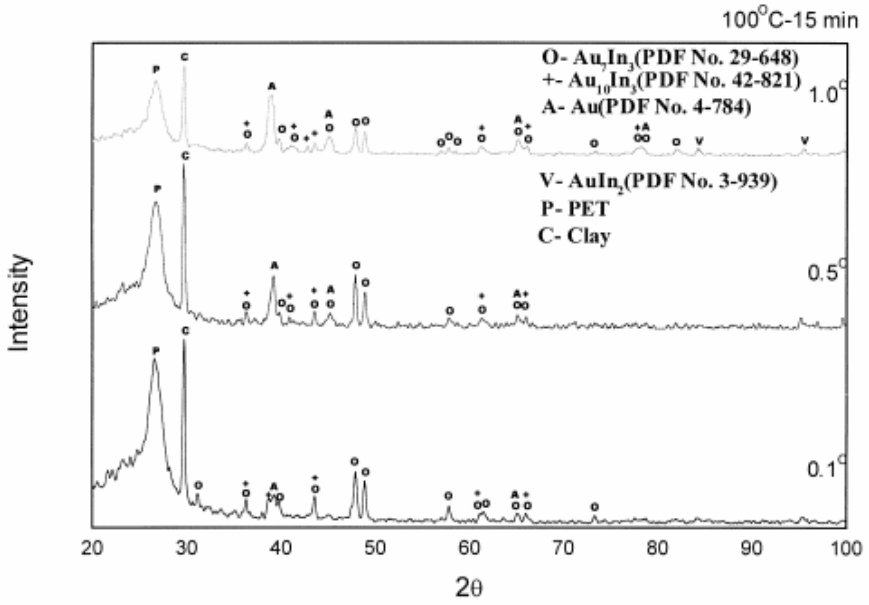

Fig. 3. Typical X-ray spectra of the Au/In microjoint hot-pressed at 100°C for 15 min, recorded at different incident angles.

and In (2 μm) before joining. In addition, two other intermetallic phases, $Au_{10}In_3$ and $AuIn_2$, were observed for the specimens prepared using solid state interdiffusion bonding, i.e. hot pressing below the melting point of In. For those specimens produced above the melting point of In, i.e. undergoing solid liquid interdiffusion bonding, the intermetallic phase Au_9In_4 was observed in the X-ray spectra. The two phases, Au_7In_3 and Au_9In_4, have similar atomic composition, and are designated as γ' and γ in the Au–In binary phase diagram [8]; however, the latter is stable only at high temperature. This result illustrates that the SLID process can form intermetallics which are different from those existed in the specimens prepared by the SSID process. When the In foil was used to form the microjoints, i.e. In is a major constituent in the microjoint, it is observed that the X-ray spectra show peaks mainly from In, with small peaks from the intermetallic $AuIn_2$.

3.3. Transmission electron microscopy of a Au/In/Au microjoint

Reactions in the Au–In diffusion couples is reported to be the fastest formation of intermetallics among transition metals and is characterized by an activation energy of 0.23 eV [9]. Consequently, preparation of thin sections for TEM observation by conventional ion milling method has been found to be invalid because ion beam induced phase transformation can readily occur. To overcome this difficulty, ultramicrotomy was utilized in the current study to prepare thin sections of the microjoints for TEM investigation.

A cross-section TEM micrograph of the Au/In/Au microjoint after the single lap tensile test is shown in Fig. 4a, which consists of a region of equiaxial grains and a portion of fractured segments. As a result of poor adhesion, the PET substrate delaminated from the Au/In/Au microjoint during ultramicrotomy. It has been demonstrated that a brittle material such as $AuIn_2$ will shatter and form periodic cracks during ultramicrotomy [10]. From the selected area diffraction (SAD) pattern shown in Fig. 4b, of an interfacial region, it is obtained that the equiaxial grains are pure In, and the fragments are identified to be $AuIn_2$. This result is the same as the conclusion of Millares et al. [11], where it is reported that the $AuIn_2$ intermetallic is the major phase in the reaction zone of the bulk Au–In diffusion couple.

Fig. 4c shows the microstructure of a region, which is expected to be under the maximum shear stress during the single lap tensile test, of the In about 10 μm away from the In–$AuIn_2$ interface. As a result of severe shear deformation, the polycrystalline In has transformed from a random orientation near the $AuIn_2$ to a texture near the center of the single lap specimen at which the

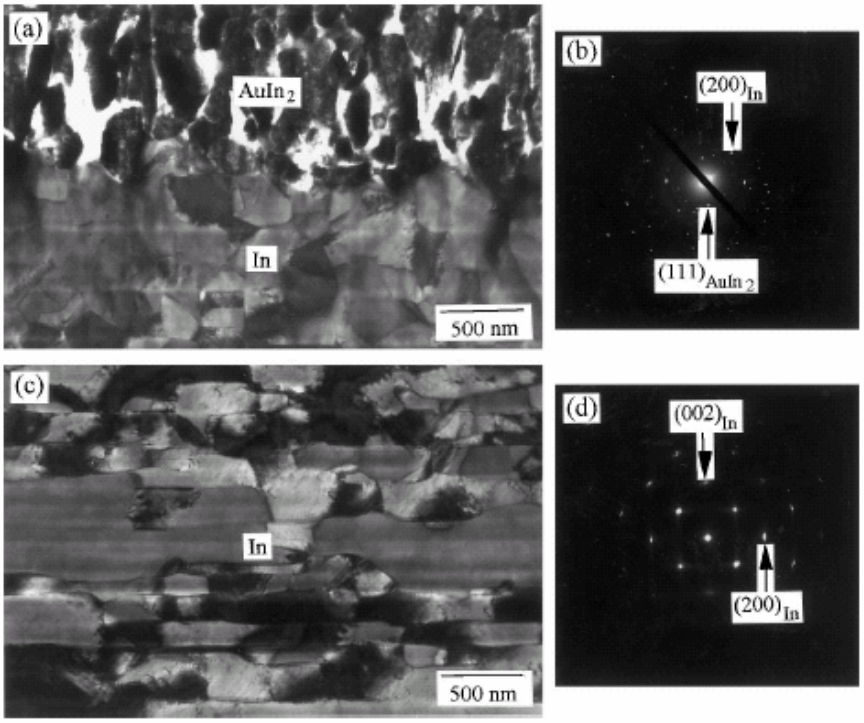

Fig. 4. (a) A cross-section TEM micrograph of the Au/In/Au microjoint after single lap tensile test; (b) the SAD pattern of an interfacial region in (a); (c) the microstructure of pure In about ~10 μm away from the In-$AuIn_2$ interface; (d) the SAD pattern of an area in (c).

shear stress reaches a maximum value. The existence of texture is illustrated both by the presence of a rectangular cell structure where high dislocation density can be readily seen in the bright field image of Fig. 4c and by the pseudo single crystal SAD pattern of Fig. 4d. The zone axis in the SAD pattern of Fig. 4d is close to the [001] direction of In that has a body-centered tetragonal crystal structure. The deformation texture consists of {110} plane oriented parallel to the substrate surface with ⟨111⟩ direction, which is the primary slip system for a body-centered cubic metal [7], aligned in the maximum shear stress.

4. Conclusions

It has been demonstrated that the shear strength of a Au–In microjoint evaluated by single lap tensile test can be improved by decreasing the thickness of the In layer and avoiding the presence of unalloyed In in the end materials. This can be achieved for example by replacing in the process In foils by In thin films.

The reaction and phase formation in the Au–In system was examined either by glancing angle X-ray diffraction or transmission electron microscopy. In the Au/In configuration where the film thickness of Au is higher than that of In, Au_7In_3 and Au are the two major phases observed in the microjoints, in addition to other intermetallics $AuIn_2$, $Au_{10}In_3$, and Au_9In_4 in small amount. On the other hand, only $AuIn_2$ and In are detected in the Au/In/Au microjoints in which In foil was used.

Acknowledgements

The authors would like to thank the National Science Council of Taiwan, for financial support of this research under contract no. NSC 88-2216-E005-004. Valuable discussions with Professors T.H. Chuang and J.C. Lin are gratefully appreciated.

References

[1] Chen YC, Lee CC. Thin Solid Films 1996;283:243.
[2] Shimizu K, Nakanishi T, Karasawa K, Hashimoto K, Niwa K. J Electronic Materials 1995;24:39.
[3] Lee CC, Wang CY, Matijasevic G. J Electronic Packaging 1993;115:201.
[4] Jacobson DM, Humpston G. Metals and Materials 1991;7:733.
[5] Berstein L, Bartholomew H. Trans Met Soc AIME 1966;236:405.
[6] Bartels F, Morris Jr. JW, Dalke G, Gust W. J Electronic Materials 1994;23:787.
[7] Dieter GD. Mechanical metallurgy (SI Metric ed.). New York: McGraw Hill, 1998.
[8] ASM handbook, vol. 3, Alloy Phase Diagrams. ASM International, 1992.
[9] Bjontegaard J, Buene L, Finstad T, Lonsjo O, Olsen T. Thin Solid Films 1983;101:253.
[10] Shieu FS, Lee WM. J Mater Sci 1997;32:6533.
[11] Millares M, Pieraggi B, Lelievre E. Solid State Ionics 1993;63–65:575.

ELSEVIER

Materials Chemistry and Physics 70 (2001) 137–143

MATERIALS CHEMISTRY AND PHYSICS

www.elsevier.com/locate/matchemphys

Characterization of the microstructure and phase formation in the Au–In system using transmission electron microscopy

Z.C. Chang, F.H. Lu, F.S. Shieu*

Institute of Materials Engineering, National Chung Hsing University, Taichung 402, Taiwan, ROC

Received 29 June 2000; received in revised form 10 August 2000; accepted 23 August 2000

Abstract

The Au–In system is of both fundamental and technical importance for engineering applications such as microelectronic packaging. The growth mechanism and crystal orientation of the Au and In thin films produced by thermal evaporation on NaCl substrates are studied by transmission electron microscopy (TEM). Like most metals, the growth of both Au and In thin films on single crystals of NaCl follows the Volmer–Weber mode, i.e. formation of metal nuclei first, and then grain growth and coalescence of the particles to form a continuous thin film. In contrast, the growth of In on the Au-coated NaCl substrates follows the Frank–van der Merwe mode, i.e. layer by layer, as a result of strong interactions between Au and In. The formation of $AuIn_2$ phase occurs instantly upon In deposition, and the intermetallic exhibits an epitaxial orientation to the underlayer Au single crystals. In addition, cross-section TEM observation of the Au/In/Au thin sections by ultramicrotomy shows that the $AuIn_2$ intermetallic is brittle.

Keywords: Growth mechanism; Intermetallic; Microstructure; Transmission electron microscopy

1. Introduction

The study of metallic thin films is of both technological importance and fundamental interest. On one hand, thin films are the key technology in many sectors of hi-tech industry, e.g. in the manufacturing of microelectronics components and solid state devices [1,2], on the other hand, they often show properties that differ from the bulk [3,4], e.g. the solubility of an impurity in a thin film is usually much higher than that in the bulk. In many applications, different types of metallic thin films need to be prepared for specific purposes. As a result, an understanding of the interactions among metals and the formation of intermetallics and their properties are crucial for the design and fabrication of solid-state devices involving thin film technology.

In a recent research conducted by Shimizu et al. [5], it is demonstrated that indium (In)-containing alloy solders have longer fatigue life, better mechanical properties and reliability than conventional tin (Sn)-containing alloys as solder interconnections for electronic packaging. Other desired properties such as thermal stability and corrosion resistance of the In-containing alloys are also reported [6–8]. It is, therefore, expected that In-containing alloys may be used in the surface mount technology for microelectronics devices in the near future. Unlike indium, gold (Au) is being widely used in the electronic industry as contact and conductor material. Reactions and characteristics of a metal–In microjoint such as Au–In need to be investigated in great detail before the engineering practice of the In-containing solders can become useful. One particular technology, so-called solid–liquid interdiffusion bonding (SLID) [9] that is drawing great attention currently for joining the die and substrate in microelectronics packaging, involves the preparation of two or more metallic thin films. One key parameter for the success of the SLID technology is control of the thickness of the metallic thin films properly.

In this study, the growth modes of Au and In thin films prepared by thermal evaporation using electrical resistance heating are investigated. Formation and mechanical properties of the $AuIn_2$ intermetallic from the Au–In bilayer are characterized by transmission electron microscopy (TEM). In addition, the effect of the Au interlayer on the orientation relationships of the In thin films deposited on the NaCl substrate, and the formation of texture in the In of the Au–In microjoints upon shear loading are discussed.

2. Experimental

Two types of specimens with different geometry were prepared to study the reactions between Au and In. In one type, single crystals of NaCl cleaved along (0 0 1) plane were

* Corresponding author. Tel.: +886-4-285-4563; fax: +886-4-285-7017.
E-mail address: fsshieu@dragon.nchu.edu.tw (F.S. Shieu).

0254-0584/01/$ – see front matter
PII: S0254-0584(00)00485-5

used as the substrate, in which Au thin films of thickness about 50 nm were first deposited on the substrate by thermal evaporation using a resistance-heated W boat. Subsequently, a thin In film of thickness about 20 nm was deposited onto the aforementioned Au-coated NaCl substrate to form an In/Au bilayer structure. The base pressure of the vacuum chamber before evaporation is $\sim 1.1 \times 10^{-3}$ Pa, and rises up to $\sim 2.7 \times 10^{-3}$ Pa during deposition. A quartz-type thickness monitor was used to measure the deposition rate, and the thickness of Au and In thin films.

In the second type of specimens, a thick Au layer of about 5 μm using thermal evaporation was deposited onto a polyethylene terephthalate (PET) substrate of dimensions 5 mm × 10 mm × 0.2 mm. Specimens for tensile test were made by sandwiching an In foil of 20 μm thick between the Au-coated PETs, and then hot-pressed in air at 250°C for 5 min. The shear strength of the Au/In/Au microjoints was evaluated by a single lap tensile test.

Microstructure of the two types of specimens was characterized by a Zeiss 902A energy filtering TEM operated at 80 kV. For the first type of specimens, thin sections were prepared by dissolving the single crystals of NaCl in distilled water and then picked up by a 300 mesh Cu grid [10]. In cases where the deposition time is short corresponding to the early stage of film growth and thus the metal film is discontinuous, a thin layer of carbon is evaporated onto the metal-coated NaCl substrates before dissolving in the water. For the sandwiched Au/In/Au specimen that has undergone tensile loading, thin sections of the failure components about 100 nm thick for cross-section TEM observation were made by a Reichert Ultracut E ultramicrotome.

3. Results and discussion

3.1. Growth of Au and In thin films on NaCl substrates

The growth modes of metallic thin films on a substrate can, in general, be classified into three categories: the Volmer–Weber mode, the Frank–van der Merwe mode and the Stranski–Krastanov mode, as shown in Fig. 1 [11]. The first mode usually occurs when the surface energy of the film materials is large compared with that of the substrate. The second and third modes, on the other hand, take place when a film of low surface energy is deposited on a substrate of high surface energy. If the strain energy in the film is small compared with the surface energy of the film material, the film will grow by the Frank–van der Merwe mechanism; if the strain energy in the film, however, is large, the Stranski–Krastanov mode will dominate.

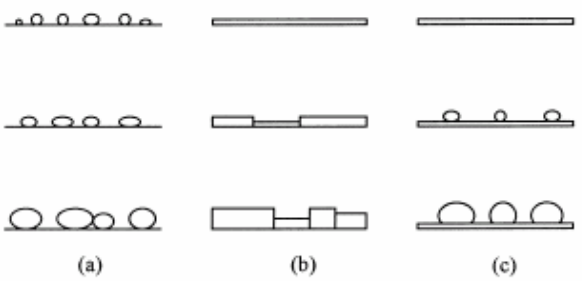

Fig. 1. A schematic of the three growth modes commonly occurring in the vapor deposition of metallic thin films: (a) Volmer–Weber mode; (b) Frank–van der Merwe mode, and (c) Stranski–Krastanov mode.

Fig. 2(a) and (b) show the morphology of Au particles deposited on a single crystal of NaCl substrate by thermal evaporation for 10 and 30 s, respectively. It can be seen from the micrograph of Fig. 2(a) that discrete Au nuclei with particle sizes ranging from 1 to 3 nm are formed at the early stage of deposition and then coalescence of the Au particles, shown in Fig. 2(b), gradually occurs as deposition continues. The Au particles grow both laterally and vertically, and eventually a continuous film of 50 nm is obtained as shown in Fig. 3(a). The bright disk-like areas in the image, within which extinction contours with four-fold symmetry are observed, reflect that the cleaved NaCl surface is full of

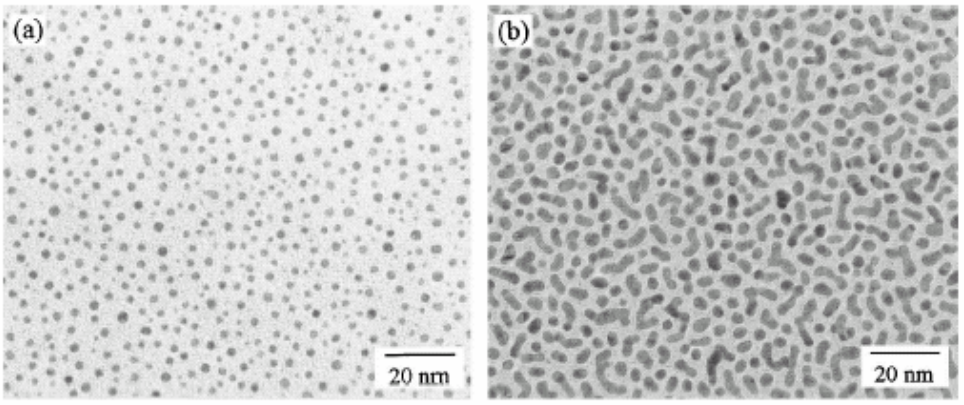

Fig. 2. Evolution of the Au thin film on single crystals of NaCl substrate during early stage of thermal evaporation: (a) formation of Au nuclei, and (b) coalescence of the Au particles upon deposition for 10 and 30 s, respectively.

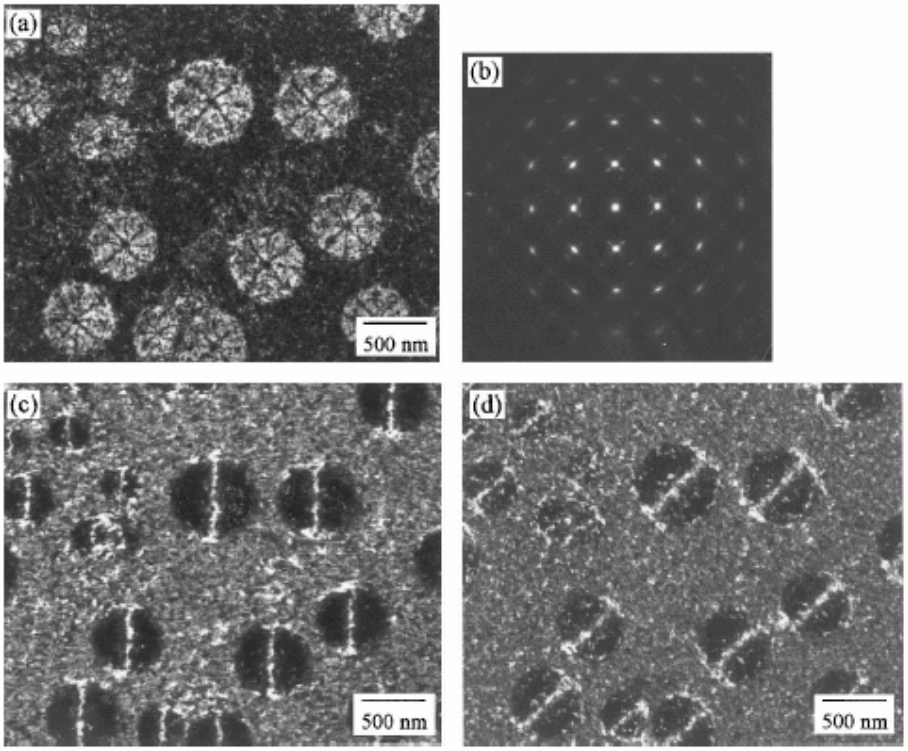

Fig. 3. TEM micrographs showing (a) the BF image, (b) the SAD pattern, (c) the (2 0 0) DF, and (d) (2 2 0) DF images, of a continuous Au film deposited on the NaCl substrate. The appearance of the bright disk-like areas in the images reflect many protrusion defects on the substrate surface.

protrusion defects [12]. A selected area diffraction (SAD) pattern of the thin film is given in Fig. 3(b), which reveals that the Au layer has an epitaxial orientation relationship with the single crystal of NaCl substrate, i.e. $(0\,0\,1)_{Au}//(0\,0\,1)_{NaCl}$ and $[0\,0\,1]_{Au}//[0\,0\,1]_{NaCl}$. The dark field (DF) images using (2 0 0) and (2 2 0) reflections are shown in Fig. 3(c) and (d), respectively, where the intersection of the two extinction contours resulting in an absorption band is easily discerned. Although the microtwins in the Au thin film are not readily defined in the bright field (BF) image of Fig. 3(a), the SAD pattern of Fig. 3(b) reveals clearly the presence of strong twin spots [12].

The BF image and SAD pattern of an In thin film of thickness of about 50 nm produced by a similar deposition condition as the Au thin film shown in Fig. 3(a) are given in Fig. 4(a) and (b). In spite of the fact that the growth mode of

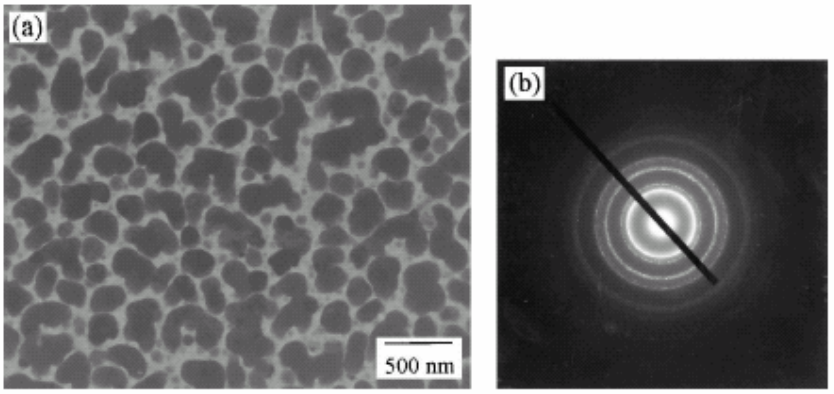

Fig. 4. TEM micrographs showing (a) the BF image, and (b) the SAD pattern of the In film having thickness similar to the Au film shown in Fig. 3, deposited on single crystals of NaCl substrate.

In on the single crystals of NaCl is similar to that of the Au on NaCl, two major differences are noted. First, within the detection limit of the thickness monitor, Au forms a continuous film but not In for the same coating thickness of 50 nm. This result is due to the surface energy of Au, 1.185 J m^{-2}, which is much higher than that of In, 0.556 J m^{-2} [13], as mentioned in the beginning of the section. As a result, the apparent growth rate of Au particles in the lateral direction is faster than that of In to reduce the total free energy of the thin film. From the cross-section viewpoint, the In particles tend to approach a sphere, whereas the Au particles favor an ellipsoid and thus form a continuous film earlier. The difference in the morphology of the metal particles is also reflected in the visibility of the microstructure of the films to the electron beam. The internal structure of the Au films can be seen in the BF image of Fig. 3(a), whereas it is almost opaque to the electron beam for the In films prepared under the same deposition condition (see Fig. 4(a)). It makes the picture even clear when the atomic scattering factor, of which the scattering power of Au is higher than that of In [12], is taken into account.

In addition, from the SAD pattern of Fig. 3(b), it is shown that the Au film is an epitaxial layer with the (0 0 1) zone axis parallel to the electron beam direction, however, the ring pattern in the selected diffraction of the In film, Fig. 4(b), indicates that it is polycrystalline. Since the lattice mismatch between In and NaCl, 42%, is much larger than that between Au and NaCl, 28%, so does the strain energy in the In thin film [11], the formation of an epitaxial relationship between In and NaCl is very likely to be obstructed.

3.2. Effect of the Au interlayer on the growth of In on NaCl substrates

Although the growth mode of both Au and In thin films on the single crystals of NaCl follows the Volmer–Weber mechanism, In undergoes a completely different growth mechanism on the Au-coated NaCl substrates. As mentioned in Section 3.1, the Au film of 50 nm thickness deposited on the single crystal of NaCl forms a continuous layer and exhibits an epitaxial orientation to the (0 0 1) NaCl substrate, i.e. $(0\,0\,1)_{Au}//(0\,0\,1)_{NaCl}$ and $[0\,0\,1]_{Au}//[0\,0\,1]_{NaCl}$, as shown in Fig. 3. The BF image and the SAD pattern of the specimen in which In of thickness of about 15 nm was deposited on the Au-coated NaCl are given in Fig. 5(a) and (b), respectively. From the electron micrographs, it can be seen that the image contrast and features of the Au in Fig. 3(a) and the In/Au bilayer in Fig. 5(a), look very similar, except that the size of disks decreases slightly in the latter case. Since the microstructure of the two specimens remains almost unchanged before and after In was deposited onto the Au films, it strongly suggests that the In must grow on the Au surface by a mechanism of Frank–van der Merwe mode, i.e. layer by layer.

Compared with the SAD pattern of Fig. 3(b) in which Au was deposited on a single crystal of NaCl, the diffraction pattern of Fig. 5(b) for In deposited onto the Au-coated NaCl is very complicated, and contains many extra spots. By careful analysis, it is found that the extra spots consist of reflections from the intermetallic phase $AuIn_2$, instead of pure In, and those due to double diffraction and microtwin, in addition to those resulting from the Au layer observed in Fig. 3(b). A close examination of the diffraction pattern in Fig. 5(b) also reveals that the (2 2 0) reflections of the $AuIn_2$ intermetallic are nearly superimposed on the Au microtwin spots. An enlargement of the microtwin reflection showing the doublet is given in the up-right corner of Fig. 5(b). Analysis of the diffraction pattern indicates that an epitaxial relationship, $[4\,0\,0]_{AuIn_2}//[2\,2\,0]_{Au}$ and $[2\,2\,0]_{AuIn_2}$ is ~7.5 away from $[2\,0\,0]_{Au}$, exists between $AuIn_2$ and Au, in which $AuIn_2$ has CaF_2 type face-centered cubic structure. A schematic of the diffraction pattern illustrating the major reflections is given in Fig. 5(c).

The instant formation of $AuIn_2$ intermetallic right after deposition of In onto Au is also observed by other investigators [14,15]. Bjontegaard et al. [14] reported that the formation and growth of $AuIn_2$ intermetallic after evaporation is characterized by an activation energy of 0.23 eV, and that the $AuIn_2$ phase is known to be the fastest transformation requiring the least thermal energy of any intermetallic among transition metals. In a study of In deposition on the Au (1 1 1) surface conducted by Robinson and Slavin [15] using Auger electron spectroscopy, it was found that the $AuIn_2$ phase was formed from the onset of deposition, and the intermetallic thickened a layer at a time, i.e. following the Frank–van der Merwe mode. In addition, the growth mode of Sn deposited onto the Au surface was investigated by Zhang and Slavin [16] using Auger electron spectroscopy, low energy electron diffraction and electron energy loss spectroscopy. It was concluded that Sn initially formed an intermetallic, AuSn, which grew laterally as a double layer, followed by continued growth of the same phase one layer at a time, i.e. the Frank–van der Merwe mode [11]. From the current experimental results and those reported in the literature, it is quite clear that strong chemical reactions or alloying among overlayers favor the Frank–van der Merwe growth mode.

3.3. Cross-section TEM of the Au/In/Au microjoints

Since the reactions between Au and In occur even at room temperature [17], preparation of thin sections for cross-section TEM investigation by conventional ion milling method has been found to be invalid due to ion beam-induced phase transformation. To overcome this difficulty, ultramicrotomy was utilized in the current study to produce thin sections of the microjoints for TEM observation.

A cross-section TEM micrograph of the Au/In/Au microjoint after the single lap tensile test is shown in Fig. 6(a), which is composed of a region of equiaxial grains and a

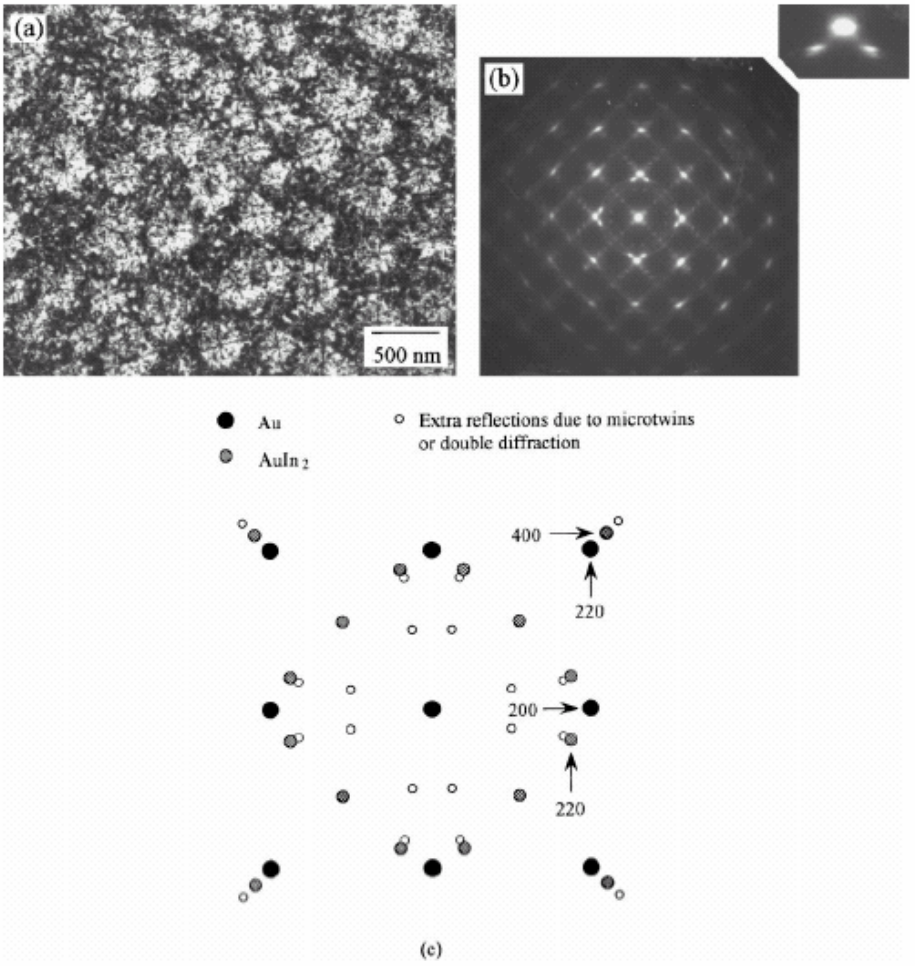

Fig. 5. TEM micrographs showing (a) the BF image, and (b) the SAD pattern of the In/Au bilayer deposited sequentially on the NaCl substrate. Inserted in the up-right corner of (b) is an enlargement of the reflection from Au microtwins. (c) A schematic indicating the origin of major reflections shown in (b).

portion of fractured segments. As a result of poor adhesion, the PET substrate delaminated from the joint during ultramicrotomy. The technique of ultramicrotomy has recently been utilized by Shieu and Lee [18] to probe the mechanical properties of a composite material. In general, a brittle material such as $AuIn_2$ will shatter and form periodic cracks during ultramicrotomy. From the SAD pattern shown in Fig. 6(b) of an interfacial region, it is deduced that the equiaxial grains are pure In, and the fragments are identified to be $AuIn_2$. This result is consistent with that reported by Millares et al. [8], who found that the $AuIn_2$ intermetallic represents the major phase in the reaction zone of a bulk Au–In diffusion couple.

Fig. 6(c) shows the cross-section microstructure of a region, near the center of the sandwiched Au/In/Au specimen, in the In foil about ~10 μm away from the In–$AuIn_2$ interface. For a single lap tensile test, the center region of the single lap specimen suffers the maximum shear stress. As a result of severe shear deformation, the polycrystalline In has transformed from a random orientation near the $AuIn_2$ to a texture near the center of the single lap specimen. The existence of texture is illustrated both by the presence of a rectangular cell structure where high dislocation density can be readily seen in the BF image of Fig. 6(c), and by the pseudo single crystal SAD pattern of Fig. 6(d). The zone axis in the SAD pattern of Fig. 6(d) is close to the [0 0 1] direction of In which has a body-centered tetragonal crystal structure. The deformation texture consists of {1 1 0} planes oriented parallel to the substrate surface with ⟨1 1 1⟩ directions, which is the primary slip system for a body-centered cubic metal, aligned in the maximum shear stress.

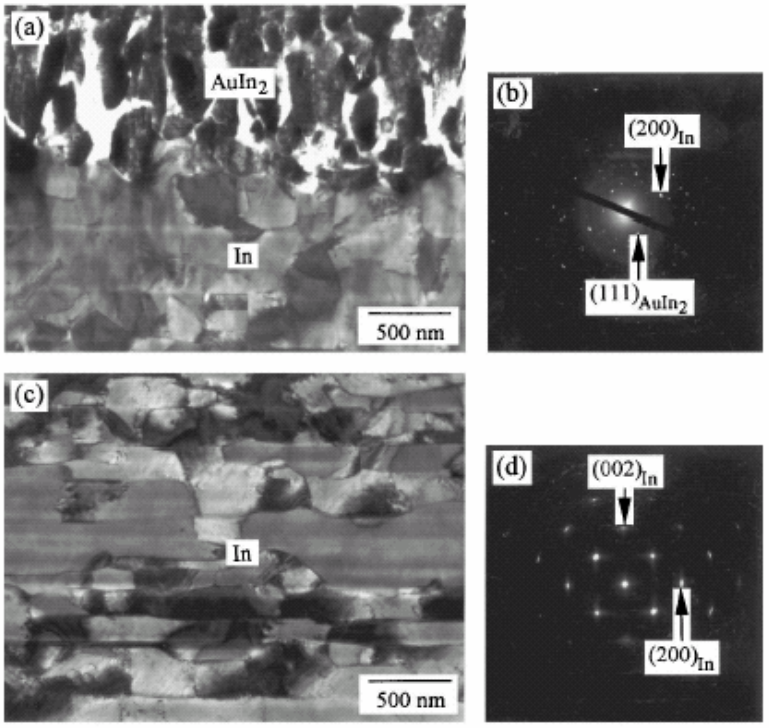

Fig. 6. (a) A cross-section TEM micrograph of the Au/In/Au microjoint after single lap tensile test. (b) The SAD pattern of an interfacial region in (a). (c) The microstructure of pure In about ~10 μm away from the In–$AuIn_2$ interface. (d) The SAD pattern of the area in (c).

4. Conclusions

It has been demonstrated that the growth mechanism of Au and In thin films deposited on the single crystals of NaCl substrate follows the Volmer–Weber mode. Unlike the In films that are polycrystalline, the Au films exhibit an epitaxial relationship, $(0\,0\,1)_{Au}//(0\,0\,1)_{NaCl}$ and $[0\,0\,1]_{Au}//[0\,0\,1]_{NaCl}$, with the single crystals of NaCl substrate. When In was deposited onto the Au-coated NaCl, it was observed that the $AuIn_2$ phase is formed instantly, and the intermetallic grows layer by layer, i.e. it follows the Frank–van der Merwe mode as a result of the strong chemical interactions between Au and In. In addition, it is found that the $AuIn_2$ layer shows an epitaxial orientation to the underlayer Au substrate. By sandwiching an In foil between two Au films, it is observed that the major phase in the microjoint is the $AuIn_2$ intermetallic. From the cross-section TEM in which thin sections were prepared by ultramicrotomy, it can be deduced that the intermetallic $AuIn_2$ is brittle in nature.

Acknowledgements

The authors would like to thank the financial support of this research by the National Science Council, Taiwan, under contract no. NSC 88-2216-E-005-004. Valuable discussion with Prof. S.L. Sass at Cornell University is gratefully appreciated.

References

[1] S.M. Sze, Semiconductor Devices: Physics and Technology, Wiley, New York, 1985.
[2] D.P. Seraphim, R. Lasky, C.Y. Li, Principles of Electronic Packaging, McGraw-Hill, New York, 1989.
[3] M.G. Hocking, V. Vasantasree, P.S. Sidky, Metallic and Ceramic Coatings: Production, High Temperature Properties and Applications, Wiley, New York, 1989.
[4] K.E. Sickafus, S.L. Sass, Acta Met. 35 (1987) 69.
[5] K. Shimizu, T. Nakanishi, K. Karasawa, K. Hashimoto, K. Niwa, J. Elect. Mater. 24 (1995) 39.
[6] D.M. Jacobson, G. Humpston, J. Elect. Mater. 19 (1991) 733.
[7] P.T. Vianco, A.C. Kilgo, R. Grant, J. Mater. Sci. 30 (1995) 4871.
[8] M. Millares, B. Pieraggi, E. Lelievre, Solid State Ionics 63–65 (1993) 575.
[9] L. Berstein, H. Bartholomew, Trans. Met. Soc. AIME 236 (1966) 405.
[10] T. Schober, R.W. Balluffi, Phil. Mag. 20 (1969) 511.
[11] E. Bauer, H. Poppa, Thin Solid Films 12 (1972) 167.
[12] P. Hirsch, A. Howie, R.B. Nicholson, D.W. Pashley, D.W. Whelan, Electron Microscopy of Thin Crystals, Robert-Krieger, New York, 1977.

[13] CRC Handbook of Chemistry and Physics, 68th Edition, CRC Press, Boca Raton, FL, 1987.
[14] J. Bjontegaard, L. Buene, T. Finstad, O. Lonsjo, T. Olsen, Thin Solid Films 101 (1983) 253.
[15] M.C. Robinson, A.J. Slavin, Phys. Rev. B 54 (1996) 14087.
[16] Y. Zhang, A.J. Slavin, J. Vac. Sci. Technol. A 9 (1991) 1784.
[17] V. Simic, Z. Marinkovic, Thin Solid Films 41 (1997) 57.
[18] F.S. Shieu, W.M. Lee, J. Mater. Sci. 32 (1997) 6533.

表 C034A 共 頁 第 頁